Icarus 410 (2024) 115698

Contents lists available at ScienceDirect

Icarus

journal homepage: www.elsevier.com/locate/icarus

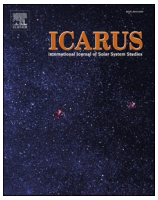

Observation of the Southern Polar cap during MY34-36 with ExoMars-TGO NOMAD LNO

L. Ruiz Lozano [a,b,*], F. Oliva [c], Ö. Karatekin [a], G. Bellucci [c], V. Dehant [a,b], E. D'Aversa [c], F.G. Carrozzo [c], F. Schmidt [d,e], G. Cruz Mermy [d], I.R. Thomas [f], A.C. Vandaele [f], F. Daerden [f], B. Ristic [f], M.R. Patel [g], J.-J. López-Moreno [h]

[a] Royal Observatory of Belgium (ROB-ORB), B-1180 Brussels, Belgium
[b] Earth and Life Institute, Secteur des Sciences et Technologies, Université Catholique de Louvain (UCLouvain), 3, Place Louis Pasteur/L4.03.08, B-1348 Louvain-la-Neuve, Belgium
[c] Istituto di Astrofisica e Planetologia Spaziali (IAPS-INAF), 00133 Rome, Italy
[d] Université Paris-Saclay, CNRS, GEOPS, Orsay, France
[e] Institut Universitaire de, France
[f] Royal Belgian Institute for Space Aeronomy (BIRA-IASB), B-1180 Brussels, Belgium
[g] School of Physical Sciences, The Open University (OU), Milton Keynes MK7 6AA, UK
[h] Instituto de Astrofisica de Andalucía (IAA), Consejo Superior de Investigaciones Científicas (CSIC), 18008 Granada, Spain

ARTICLE INFO

Keywords:
Mars
Mars, polar caps
Spectroscopy
Ices, IR spectroscopy

ABSTRACT

Mainly designed to study minor atmospheric species in the Martian atmosphere, the Nadir and Occultation for MArs Discovery (NOMAD) instrument suite onboard the 2016 ExoMars Trace Gas Orbiter (TGO) can also be exploited for surface ice detection. In this work, we investigate the nadir observations of the NOMAD infrared channel from the Martian Years 34 to 36 (Mars 2018 to December 2022), especially for CO_2 ice detection. Based on Oliva et al. (2022), we present an updated method taking advantage of the 2.7 μm absorption band for surface ice detection by selecting the diffraction orders 190, 169, 168 and 167. We focus the analysis on the Southern polar cap and define its boundaries during its sublimation phase in MY34–36. Globally, seasonal changes seem repeatable for MY34–36. Moreover, we show the potential of the 2.29 μm absorption band for surface CO_2 ice identification through the diffraction order 193. We define a pseudo-band depth as a good proxy for CO_2 ice detection. Following a semi-qualitative approach, we attempt to reproduce such spectra by using the Planetary Spectrum Generator (PSG) model in order to estimate CO_2 ice equivalent grain size. For the selected periods, the estimations are in the order of centimetres, which is in agreement with previous studies using spectral observations of OMEGA, CRISM and TES instruments.

1. Introduction

Historically, the Martian polar caps have been observed from Earth for more than a century (ground based observations and documentations reported in Fischbacher et al., 1969; Dollfus, 1973; Iwasaki et al., 1986; James et al., 1987; James et al., 1990; Benson and James, 2005) and, in 1969, NASA Mariner 6 and 7 spacecrafts directly observed the recession of the Southern polar cap. For the first time, the twin satellites identified CO_2 ice as its major component (Herr and Pimental, 1969). In the late 1970s, the Viking landers made the first efforts in measuring the pressure variations on the surface of Mars during a whole Martian year (MY). These variations, estimated to be over 25%, were found to be directly linked to the atmospheric CO_2 cycle (Hess et al., 1979, 1980). Indeed, the Martian atmosphere is strongly controlled by the seasonal changes in the polar cap deposits, resulting from the sublimation and condensation processes of CO_2 (Kieffer, 1979). These CO_2 exchanges between the atmospheric layers and the solid planet alter the atmospheric angular momentum (Karatekin et al., 2011) and impacts even the rotation of the solid planet at seasonal time scales (up to 0.4 milliseconds in Length-of-Day, Cazenave and Balmino, 1981; Defraigne et al., 2000; Van den Acker et al., 2002; Karatekin et al., 2006; Konopliv et al., 2011). Therefore, observing the seasonal and inter annual variabilities of CO_2 ices on the

* Corresponding author at: Royal Observatory of Belgium (ROB-ORB), B-1180 Brussels, Belgium.
E-mail address: luca.ruizlozano@oma.be (L. Ruiz Lozano).

https://doi.org/10.1016/j.icarus.2023.115698
Received 28 March 2023; Received in revised form 26 June 2023; Accepted 7 July 2023
Available online 8 July 2023

Martian surface is important for understanding the CO_2 cycle, which drives the current atmospheric dynamics in close connection with water and dust cycles (Karatekin et al., 2005, 2011; Dehant et al., 2020). The variability of Martian atmospheric dynamics provides insight into the planet's global atmosphere and its long-term evolution (Lange et al., 2022).

Several orbiter missions have deeply analysed the Martian CO_2 ice in different spectral ranges: Mars Global Surveyor TES (Christensen et al., 2001), Mars Odyssey THEMIS (Christensen et al., 2004), Mars Express OMEGA (Bibring et al., 2004a) and PFS (Formisano et al., 2005) spectrometers and the Mars Reconnaissance Orbiter CRISM (Murchie et al., 2007) and MARCI instruments (Bell et al., 2009). Spectrally active in the infrared spectral range, CO_2 ice has been observed at the poles (Kieffer et al., 2000; Titus and Kieffer, 2002; Langevin et al., 2007; Pelkey et al., 2007; Appéré et al., 2011; Brown et al., 2010, 2014; Schmidt et al., 2009, 2010), and also as ice clouds in the mesosphere (at altitudes above 50 km) at equatorial latitudes (Formisano et al., 2006; Montmessin et al., 2006, 2007; Clancy et al., 2007; Määttänen et al., 2010; Vincendon et al., 2011; Liuzzi et al., 2021). Moreover, using this spectral range allowed to distinguish CO_2 and H_2O ices as they present different IR spectral signatures (Bibring et al., 2005). On the other hand, forward models (Singh and Flanner, 2016) and radiative transfer models of IR reflectance spectra (Hapke, 1981; Andrieu et al., 2018) provided information on the CO_2 ice microphysical properties, such as the grain size, the layer thickness and the icy mixture composition (Langevin et al., 2007; Brown et al., 2010, 2014; Appéré et al., 2011).

Since March 2018, ExoMars-Trace Gas Orbiter NOMAD, mainly designed for the study of trace gases, atmospheric aerosol abundances and Martian climatology (Neefs et al., 2015; Vandaele et al., 2015a, 2018; Thomas et al., 2016), has been providing IR observations of Mars at high spectral resolution. Oliva et al. (2022) demonstrated that the NOMAD nadir IR channel can also be exploited to study surface CO_2 ice. Using a semi-qualitative approach, they studied the respectively narrow and strong CO_2 ice absorption bands at 2.35 μm and 2.7 μm over MY34–35. They obtained CO_2 ice seasonal-latitudinal maps in good agreement with the Mars Climate Database v6.1 (MCD) predictions (Forget et al., 1999; Millour et al., 2018) and with the OMEGA spectrometer observations (Schmidt et al., 2009, 2010; Appéré et al., 2011). They hence opened a new possibility of surface science with NOMAD.

In direct continuation of Oliva et al. (2022), in this work, we further explore the NOMAD nadir data set information content by focusing the analysis on the Southern polar cap. Following a qualitative approach, we present an updated method based on the characterisation of the 2.7 μm ice absorption band in order to detect the presence of surface ice. We also analyse the seasonal and inter annual changes of the southern polar cap during 3 Martian Years. Nevertheless, this band is not suitable for the identification of CO_2 ice due to the overlapping signal of water ice. Therefore, we use the 2.29 μm absorption band for CO_2 ice detection and discuss the potential of this band for grain size retrieval.

We present in Section 2 and 3 a brief description of the NOMAD instrument and the nadir observations used in this study. Then, we describe the methodology and perform the analysis of NOMAD nadir data for MY34–36 in Section 4. Finally, the results are discussed and compared to previous studies in Section 5.

2. NOMAD instrument

The Nadir and Occultation for MArs Discovery (NOMAD) instrument is a suite of three high resolution spectrometers that was selected as part of the payload of the 2016 ExoMars Trace Gas Orbiter (TGO) mission. Led by the Royal Belgian Institute for Space Aeronomy (BIRA-IASB), NOMAD has been observing the Martian atmosphere since March 2018 ($L_S = 150^\circ$ in MY34) through three channels, one operating in the ultraviolet-visible spectral range (UV-VIS) and the two others in the infrared (IR). A first spectrometer is devoted to solar occultation observations (SO channel). A second spectrometer is capable of performing nadir, limb, and solar occultation observations (LNO channel). Both spectrometers cover the near IR spectral range. On the other hand, a third spectrometer (UVIS channel) can work in the three observation modes covering the UV-VIS spectral range. A complete description of the instrument can be found in the following papers: Neefs et al. (2015), Vandaele et al. (2015a), Vandaele et al. (2015b), Thomas et al. (2016) and Patel et al. (2017).

To study surface ice, we select the LNO channel providing nadir observations with a typical integration time of around 200 ms. This channel covers the 2.3–3.8 μm IR spectral range with a spectral resolution of 0.3 cm^{-1} (Liuzzi et al., 2019). From the TGO orbit, the LNO ground track footprint is defined as an elongated rectangle of 0.5 km by 17.5 km, allowing to map most of the surface of the planet every 30 sols (Thomas et al., 2016). The NOMAD LNO spectrometer has the particularity of not observing the entire spectral range at once. The data are acquired in 22 cm^{-1} wide spectral windows. These small portions, (hereafter referred as spectral orders) represent specific diffraction orders of the diffraction grating. Each LNO observation can select a maximum number of 6 diffraction orders every 15 s, in order to ensure the best possible signal-to-noise ratio (SNR).

The selection of different orders is obtained by appropriately adjusting the frequency of the entrance Acousto-Optical Tunable Filter (AOTF) (Liuzzi et al., 2019) through an internal radio-frequency generator. As a result, the general shape of the LNO raw spectra is strongly affected by the AOTF transmission and by the spectral response of the grating, i.e., the Blaze function (defined by a sinc-squared function, Liuzzi et al., 2019). On the other hand, the AOTF is characterised by a strong peak with several side-lobes, and can be represented by a combination of a sinc-squared function with a Gaussian curve (Liuzzi et al., 2019). Considering the secondary peaks in the AOTF curve, it is worth noting that photons incoming from outside the selected spectral range can fall on the grating. An unexpected signal is hence summed with the expected spectral information and can become significant on the edges of each order (see Section 5.3.2).

For this work, we use spectrally and radiometrically calibrated LNO data converted into a reflectance factor. The reflectance factor R_λ is defined as the LNO radiance divided by the measured Solar irradiance at Mars and by the cosine of the solar zenith angle (SZA). Therefore, the LNO reflectance factor defined at wavelength λ can be written as

$$R_\lambda = \frac{1}{cos(SZA)} \frac{\pi L_\lambda}{\Phi_\lambda d_{Mars}^2} \quad (1)$$

where L_λ is the LNO measured spectral radiance (W m^{-2} sr^{-1} μm^{-1}), Φ_λ is the Solar flux at 1 AU, d_{Mars} is the Sun–Mars distance in AU, and finally *SZA* is the solar zenith angle. All details about the spectral and radiometric LNO calibration can be found in Liuzzi et al. (2019), Cruz Mermy et al. (2022) and Thomas et al. (2022). It is important to note that the AOTF and Blaze modulations also propagate to the reflectance factor conversion in the form of low-frequency oscillations in the spectral continuum. For this reason, we exclude the reflectance factors at the outer parts of each spectral order in order to mitigate these oscillations (see Section 4 and 5.3.3).

Thomas et al. (2016) identified the instrumental thermal background as the main source of noise, limiting the integration times in order to avoid the saturation of the detector. As already mentioned, the 15 s period of observations is divided by the number of orders (maximum of 6). The SNR hence increases with fewer orders. Typically with LNO, two or three orders are measured in the same sequence of observations. The SNR generally takes values around 8–10. For the best scenario, i.e. when the SZA is around zero (when the Sun is directly overhead), the SNR is expected to be around 15–20. As a comparison, spectrometers dedicated for surface study, such as OMEGA and CRISM, present a SNR higher than 100 (Bibring et al., 2004a; Murchie et al., 2007).

3. Dataset

During an acquisition, NOMAD alternates observations according to orders planned several weeks in advance. The choice of orders depends on several factors, such as their main focus (i.e. different gas, dust, surface) and the limitations of the instrument (see Section 2). Moreover, the LNO channel has reduced instrument sensitivity at the wavelengths above 2.8 μm. This results in a low SNR. Therefore, not all orders are used with the same frequency of observation, making the available wavelength ranges highly dependent on such strategy. Therefore, this affects the spatial and temporal coverage of the orders, i.e. the availability of the observations for this study.

As already described in Oliva et al. (2022), CO_2 ice exhibits several features in the LNO spectral range, which are covered by different orders (see Fig. 1). Panel A shows a simulated CO_2 ice albedo spectrum (in blue) using the Planetary Spectrum Generator (PSG) tool (see Section 5.3, Villanueva et al., 2018), while Panel B gives its imaginary refractive index, describing the absorption coefficient in the LNO spectral range (Hansen, 2005). For comparison, both panels show H_2O ice spectra in the LNO spectral range (in black). Due to the low SNR, the CO_2 ice absorption bands above 2.8 μm in Fig. 1 are poorly covered by NOMAD in MY34–36. Few observations are made, leading to limited surface coverage over the Southern polar cap. For these reasons, these wavelengths are not included in this work.

Regarding the 2.7 μm absorption band, the strongest in the LNO range, it is important to mention that water ice also presents spectral features at this wavelength (see Fig. 1B). Moreover, this band can easily be saturated, especially in the presence of a thick ice layer. As shown in Fig. 1A, orders 169 (2.612–2.632 μm), 168 (2.627–2.648 μm) and 167 (2.643–2.664 μm) cover the short-wavelength shoulder of the strong 2.7 μm ice absorption band. Order 169 has been already used in a spectral ratio with order 190 (2.323–2.341 μm) for surface ice detection (Ice Index; Oliva et al., 2022). Indeed, as order 190 falls into the continuum range, these two orders allow an estimation of the intensity of the 2.7 μm band. Regarding orders 168 and 167, Ruiz Lozano et al. (2022) discussed their potential to be used for surface ice detection, but also for more transient phenomena such as ice clouds thanks to a particular combination of these orders.

On the other hand, Oliva et al. (2022) have already proven that the 2.35 μm absorption band, widely used for the LNO observations (order 189: 2.335–2.354 μm, see Fig. 1A), is never saturated and offers an interesting opportunity for the detection of CO_2 ice and the retrieval of its microphysical properties. In addition to the analysis of surface ice in the polar regions, they have discovered CO_2 ice signatures at low latitudes. After several considerations, the CO_2 ice clouds hypothesis is the most likely scenario.

Compared to Oliva et al. (2022), the narrow band at 2.29 μm covered by order 193 (2.286–2.305 μm, see Fig. 1A) has been considerably used in MY35 and 36. This order turns it into a new candidate for the CO_2 ice study, given the high number of observations made and good instrument sensitivity.

Considering the different points listed above, we investigate, in this work, the information content of the LNO observations through orders 169, 168, 167 (the 2.7 μm ice absorption band) combined with order 190 (continuum part) and order 193 (the 2.29 μm CO_2 ice absorption band). The time coverage is over MY34–36, starting at $L_S = 150°$ in MY34 (start of the science phase, March 2018) to $L_S = 360°$ in MY36 (December 2022), for orders 169, 168, 167 and 190. On the other hand, order 193 covers only MY35–36 (March 2019 to December 2022), as there is no LNO observation with this order in MY34. We exclude LNO

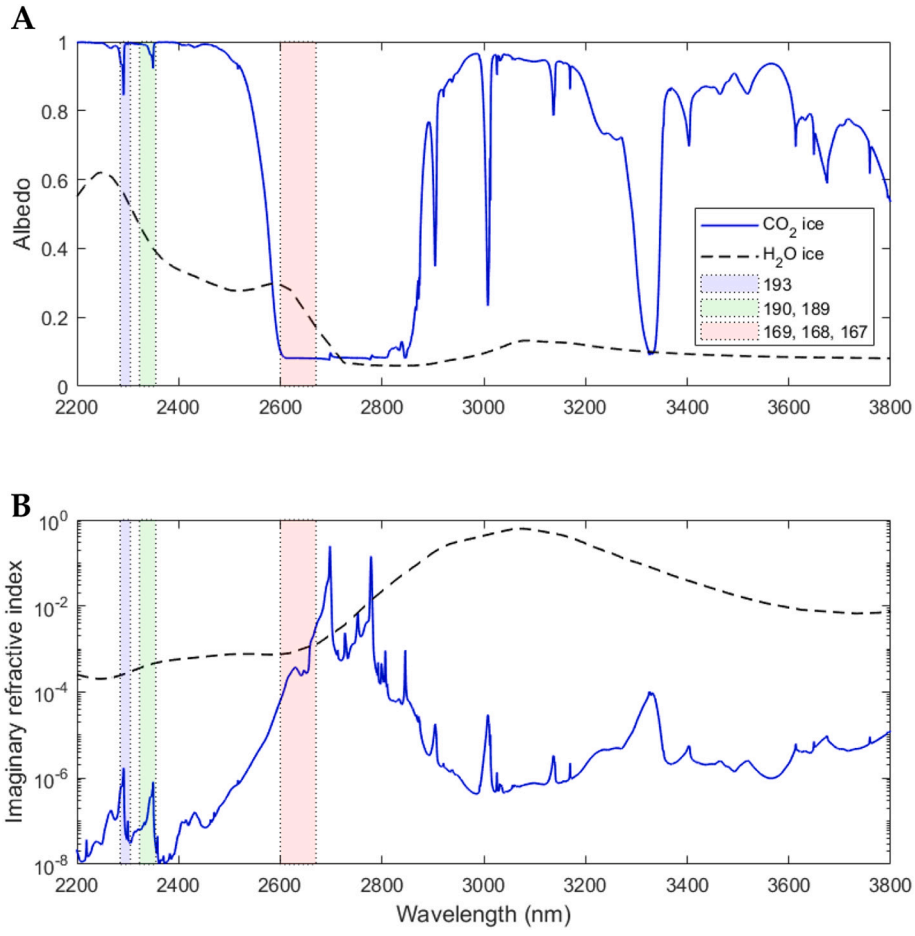

Fig. 1. (A) Simulated CO_2 ice (solid blue line; equivalent grain size of 10 mm, see Section 5.3) and H_2O ice (dashed black line, equivalent grain size of 0.3 mm) albedo spectra using the Planetary Spectrum Generator (PSG) tool (see Section 5.3, Villanueva et al., 2018) over the LNO spectral range. The different orders mentioned in the text (orders 167, 168, 169, 189, 190 and 193) are highlighted in blue, green and red (see figure legend). (B) Imaginary refractive index for CO_2 ice (Hansen, 2005) and H_2O ice (Warren and Brandt, 2008) describing the absorption coefficient over the LNO spectral range. Same legend as panel A. (For interpretation of the references to colour in this figure legend, the reader is referred to the web version of this article.)

observations with a SZA larger than 75°, as the signal intensity reaching NOMAD is strongly affected by large illumination angles. Therefore, we remove SNRs below ~8.

As we focus the analysis on the Southern polar cap, it is worth noting that the results should not be affected by the presence of the Polar Hood clouds. As they are composed of water ice (Benson et al., 2010; Wolff et al., 2019), only the 2.7 μm band would be suitable for their detection. Nevertheless, their microphysical properties do not strongly influence the spectral absorption bands compared to the extensive, abundant and thick surface ice deposits that characterise the cap. Due to the low SNR of the instrument, the Ice Index is unable to detect them (more details in Oliva et al., 2022 and Ruiz Lozano et al., 2022).

4. Methodology

4.1. Ice detection through the 2.7 μm absorption band

In this section, we focus the analysis on the short-wavelength shoulder of the 2.7 μm band. As already mentioned in Section 3, this band cannot be used to distinguish CO_2 ice from H_2O ice. Nevertheless, it can easily detect abundant surface ice deposits, as it has been proved with the Ice Index in Oliva et al. (2022) using a spectral ratio between orders 190 and 169. It is important to note that the number of nadir acquisitions using order 169 decreased significantly during MY35 and MY36. This hence affects the observation of the southern polar cap. In order to take into account the best spatial and temporal coverage to build a seasonal map, we adapt the Ice Index by considering also the ratios between orders 167 and 168 and order 190. It is worth noting that, in nadir mode, the main source of variability in the reflectance factors comes from the surface albedo variations resulting from different Martian surface mineralogy absorptions (Christensen et al., 2001; Vivian et al., 2014; Riu et al., 2019). Therefore, normalising the LNO reflectance factor to a Martian albedo allows to remove spatial albedo variations over the whole Martian surface. For each order, we define the LNO_{Norm} ratio (Ruiz Lozano et al., 2022) as R/TES, where R is the LNO reflectance factor value taken at the centre of the selected order (see Section 2), and TES is the MGS-TES bolometric Martian albedo (0.3 to 2.9 μm) (Christensen et al., 2001). Both R and TES are zonally averaged in each considered L_S-latitude bin of the selected order. Then, we compute the New Ice Index (NII) as

$$NII = \frac{1}{3} \times \left(\frac{LNO_{Norm}190}{LNO_{Norm}169} + \frac{LNO_{Norm}190}{LNO_{Norm}168} + \frac{LNO_{Norm}190}{LNO_{Norm}167} \right) \quad (2)$$

We apply the NII to the LNO data and construct a latitudinal-seasonal map in order to analyse the seasonal ice coverage (see Fig. 2). LNO data are organised in terms of latitude (from 90°N to 90°S) and time (solar longitude, L_S) binned 1° by 1°.

As we can see in Fig. 2, high NII values are present at the highest probed latitudes. They represent the sublimation and condensation phases of the northern polar cap (L_S ~ 0° - 25° in panel B and C, and L_S

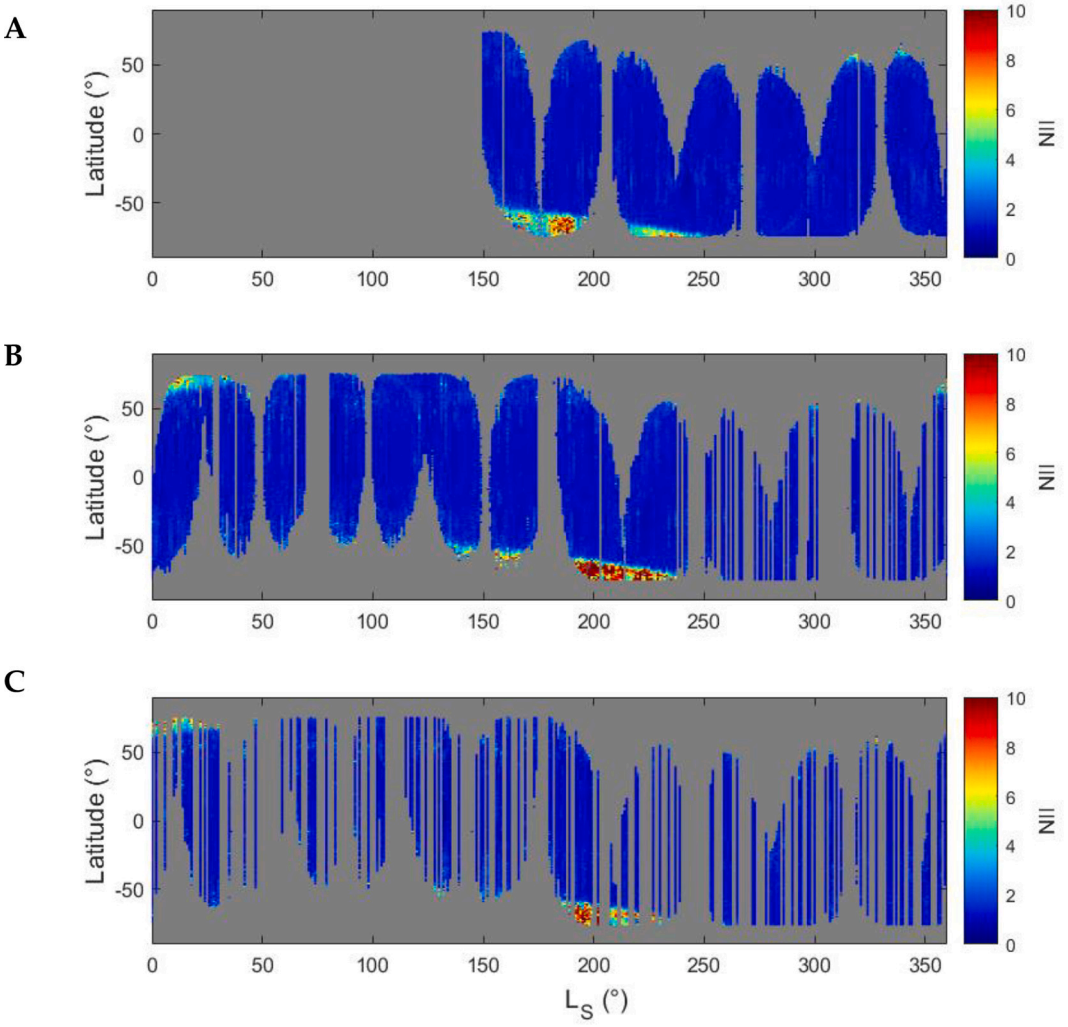

Fig. 2. Latitudinal-seasonal map of NII binned 1° by 1°. Latitudes range from −90° to 90°. By definition, the highest NII values indicate the presence of surface ice. (A) LNO observations cover MY34, from L_S = 150° to 360°, with a SZA < 75°. (B) Same for all MY35. (C) Same for all MY36.

~ 310° - 360° in panel A respectively) (Cull et al., 2010; Brown et al., 2012; Hansen et al., 2013) and the sublimation phase of the southern polar cap (L_S ~ 150° - 250° in the three panels) (Piqueux et al., 2003; Langevin et al., 2007; Schmidt et al., 2009, 2010; Brown et al., 2010, 2014; Oliva et al., 2022), better covered with respect to the North. For that reason, we focus the analysis on the South only (see Section 5). It is interesting to notice that MY34 covers the 2018 global dust storm from L_S ~ 180° to 250° (Viúdez-Moreiras et al., 2019; Gillespie et al., 2020). As discussed in Oliva et al. (2022), high dust abundances occurring during a global dust storm reduce the 2.7 μm ice absorption band, impacting its effectiveness in the identification of the ice. Nevertheless, the NII is still able to detect the polar cap at the South pole during this period, as shown in Fig. 2A (see also Section 5.1).

4.2. CO_2 ice detection through the 2.29 μm absorption band

In order to identify CO_2 ice, this section concerns the analysis of the 2.29 μm CO_2 ice absorption band, covered by order 193 (see Fig. 3). Being the band centred in this order, it has the advantage of being less affected by instrumental response modulations, with respect to the 2.35 μm absorption band used in Oliva et al. (2022) (see Fig. 1).

In order to study the 2.29 μm absorption band, we rely on a band depth analysis. The same approach already succeeded to identify the diversity of the Martian surface mineralogy (Bell et al., 2000; Murchie et al., 2000; Bibring et al., 2004b; Gendrin et al., 2005; Langevin et al., 2005a, 2005b; Pelkey et al., 2007). Pelkey et al. (2007) already defined a band depth by selecting wavelength at 2.25 μm and 2.35 μm, and centred on the 2.29 μm CO_2 ice absorption band, but since NOMAD LNO works with small spectral ranges, we here adapt the band depth computation. By keeping the same formulation as Pelkey et al. (2007), we select other wavelengths. Therefore, the 2.29 μm band depth (BD2292) is defined, in this work, as

$$BD2292 = 1 - \frac{R2292}{R2292^*} = \frac{R2292}{a \times R2288 + b \times R2296} \quad (3)$$

where $R2292$ is the LNO reflectance factor value at the centre of the band (2.292 μm) and $R2292^*$ is derived from the continuum fit across the band. $R2292^*$ is defined as $a \times R2288 + b \times R2296$, where $R2288$ and $R2296$ are the LNO reflectance factor values at the wavelengths 2.288 μm (left side of the band) and 2.296 μm (right side of the band) respectively, and finally $a = 1 - b$ and $b = \frac{\lambda_{2292} - \lambda_{2288}}{\lambda_{2296} - \lambda_{2288}}$ (see Fig. 3A).

It is worthwhile to mention that the adapted BD2292 is defined as a pseudo-band depth, since $R2288$ is not totally outside the absorption band. It can be seen as a proxy for CO_2 ice, which qualitatively estimates the CO_2 ice presence and abundance. In general, as shown in Fig. 3B, band depth varies with the abundance of the absorbing component and its particle size (Clark and Roush, 1984; Langevin et al., 2007; Pelkey et al., 2007; Brown et al., 2010, 2014; Appéré et al., 2011).

On the other hand, dust and water ice impurities can also affect CO_2 ice spectra and hence, the BD2292 estimation (Pelkey et al., 2007; Bernard-Michel et al., 2009; Andrieu et al., 2018). For that reason, we investigate the impurities effect in Fig. 4 by using the PSG model (see Section 5.3.1). Globally, the increase in the H_2O ice amount tends to produce a decrease in the spectral albedo values, as H_2O ice presents a broadband absorption at these wavelengths (see Fig. 1). It becomes significant at 2.296 μm by adding 20% of H_2O ice. Nevertheless, this variation is not as pronounced at 2.292 μm (see Fig. 4A). On the other hand, dust appears brighter in the IR spectral range. Increasing its percentage hence raises the spectral albedo values in order 193. This time, we observe most of the changes at 2.292 μm, reducing the band depth (see Fig. 4B). Although the two aerosols have opposite effects on the CO_2 ice spectrum, by definition they affect the BD2292 estimation in the same way (see Eq. 3). In conclusion, both significant amounts of H_2O ice or dust impurities will underestimate the BD2292 estimation (see Fig. 4C). In other words, they will conceal the CO_2 ice signature.

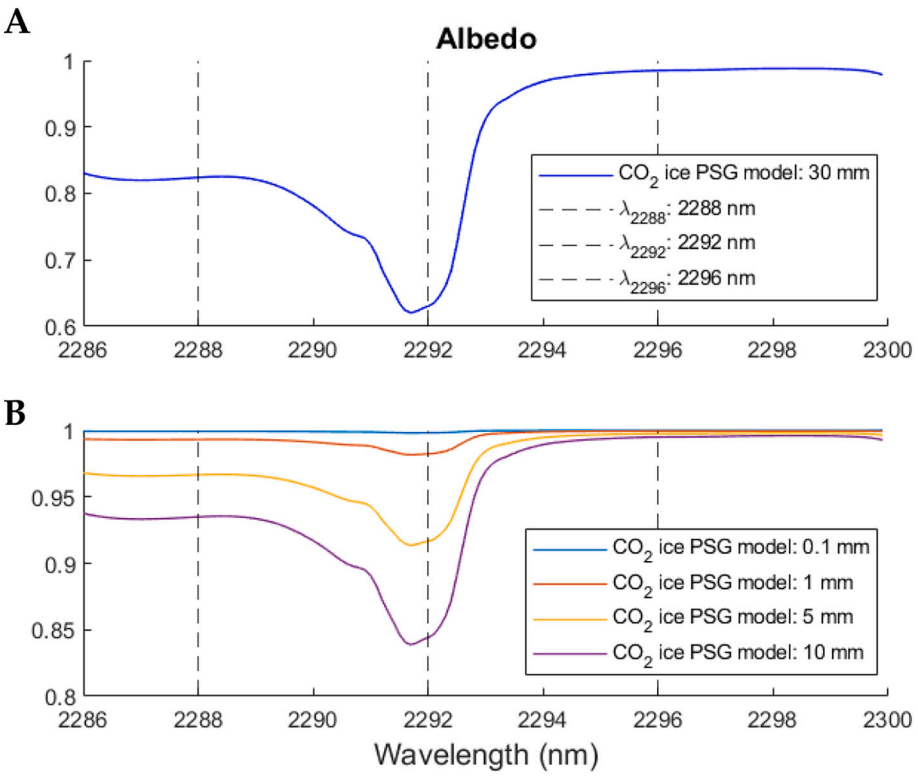

Fig. 3. CO_2 ice albedo spectra simulated with PSG model for order 193. CO_2 ice absorption band is visible at 2292 nm. Vertical dashed lines indicate the selected wavelengths for BD2292. (A) CO_2 ice equivalent grain size of 30 mm. (B) Effect of the CO_2 ice equivalent grain size on the band depth assuming a value of 0.1 mm, 1 mm, 5 mm and 10 mm.

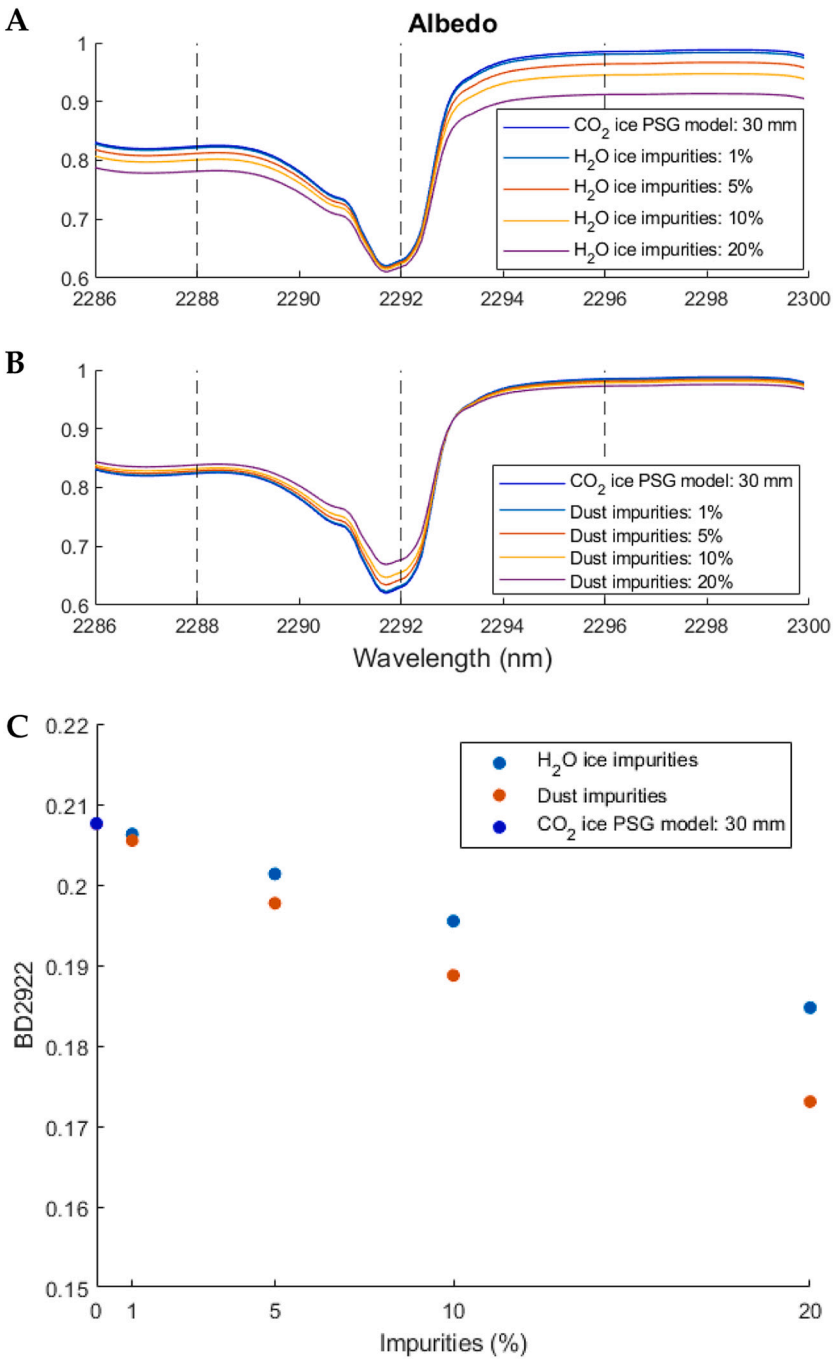

Fig. 4. CO_2 ice albedo spectra simulated with PSG model for order 193. CO_2 ice absorption band is visible at 2292 nm. Vertical dashed lines indicate the selected wavelengths for BD2292. (A) Effect of the H_2O ice contamination on the band depth assuming impurities of 1%, 5%, 10% and 20%. (B) Same with dust impurities. (C) Effect of impurities on the BD2292 estimation.

Similarly to Fig. 2 in Section 4.1, we apply the BD2292 to the LNO data set and construct a CO_2 ice latitudinal-seasonal map in Fig. 5 covering all MY35 and 36 (no LNO data in MY34, see Section 3). Although the spatial coverage is more limited than with NII (see Fig. 2), BD2292 is able to detect the sublimation ($L_S \sim 30°$ to 30° in the North and $L_S \sim 150°$ to 250° in the South) and condensation ($L_S \sim 300°$ to 360° in the North) phases of the CO_2 ice polar deposits (Oliva et al., 2022). It is interesting to note the different range of BD2292 values between the Northern (starting at L_S 0°) and Southern (starting at $L_S \sim 150°$) sublimation phases. Regarding the North Pole, it is extremely rare to find pure CO_2 ice during the recession. In fact, H_2O ice mainly composes the surface of the northern polar cap, which obscures the seasonal CO_2 ice layer. While CO_2 ice distribution is inhomogeneous during early spring (Ls ~ 0° - 30°), a H_2O ice annulus is present at latitude 50°N (Brown et al., 2012). This hence has an impact on the BD2292 estimation, as seen in Fig. 4C. On the other hand, the Southern polar cap is known to be composed of clean thick CO_2 ice slabs in winter and fine-grained CO_2 ice during the spring at its edges (Langevin et al., 2007). Therefore, strong CO_2 ice signatures are represented by the highest BD2292 values. Nevertheless, we observe smaller BD2292 values around L_S 200°. During this period, H_2O frost contamination has been observed over the seasonal cap, occulting the CO_2 ice signatures at latitudes above 75°S (Langevin et al., 2007; Appéré et al., 2011), and hence impacting the BD2292 estimation (see Fig. 4C).

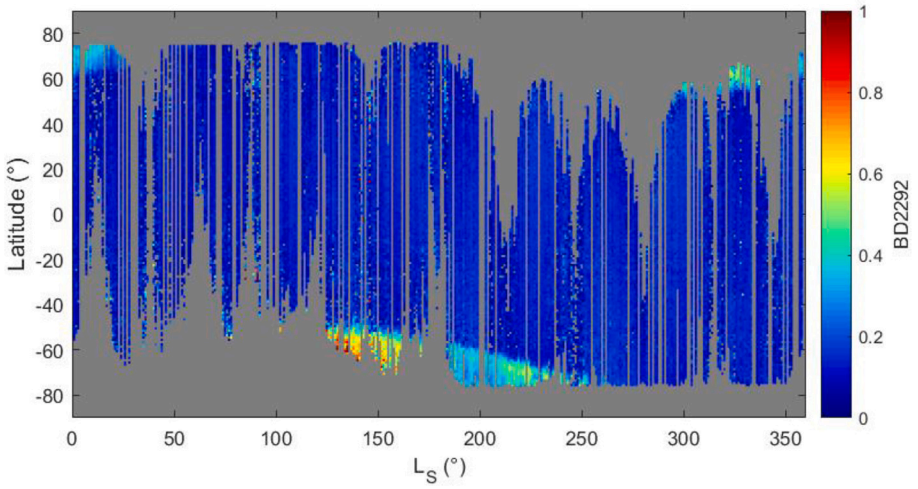

Fig. 5. Latitudinal-seasonal map of BD2292 binned 1° by 1°. LNO observations cover all MY35 and 36 for a SZA < 75°.

5. Results and discussion

5.1. South Polar cap edges

In this section, we qualitatively discuss the possible inter annual changes of the Southern polar cap for MY34–36. To do that, we estimate the extension of the polar cap deposits through the latitudinal-seasonal trend by using the NII for the best temporal coverage (see Fig. 2).

As in Oliva et al. (2022), we define the edge of a cap at a given L_S as the latitude where the NII values suddenly increase with respect to the mean value obtained for the equatorial regions (see Fig. 6).

We apply this criterion on the map shown in Fig. 2 for the South Pole and compare its recession for MY34–36. The results are presented in Fig. 7A. The comparison with the MCD v6.1 CO_2 ice column density is purely qualitative. Indeed, our polar cap boundaries should be considered as an indication of abundant ice, and not as an ice transitional region. We hence do not attempt to perform a quantitative retrieval of the ice abundance. As we can see in Fig. 7A, MY36 is the year with the lowest spatial coverage, which may challenge the comparison with the two other years. Nevertheless, before $L_S = 170°$, the few blue points seem to follow the trend of MY34 and 35. Seasonal variations in the three Martian Years globally show a correlation for that period.

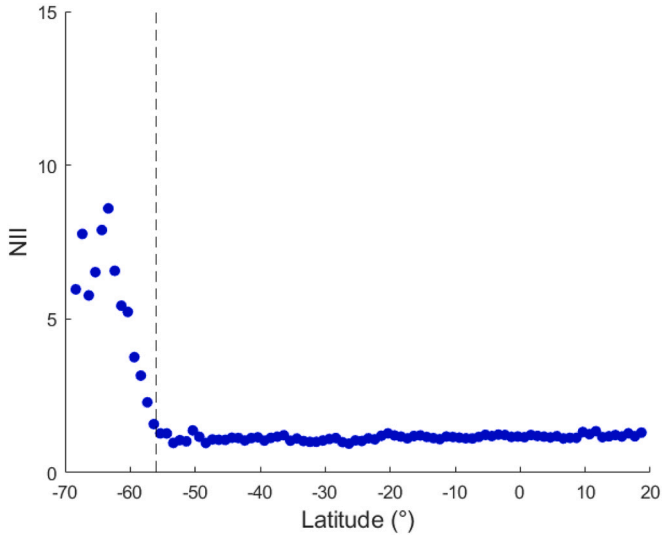

Fig. 6. Latitudinal trend of the NII for $L_S = 180°$ (MY34). The vertical dashed black line indicates the latitude in which the NII values suddenly increase due to the presence of the seasonal cap.

As already mentioned in Section 4.1, MY34 covers the 2018 global dust storm from $L_S \sim 180°$ to 250° (Viúdez-Moreiras et al., 2019; Gillespie et al., 2020), impacting the ice detection (see Fig. 2A). For that reason, we compare our boundaries definition for MY34 with the CO_2 ice column density of the Laboratoire de Météorologie Dynamique Global Climate Model (LMD GCM) using the MY34 dust activity (see Fig. 7B) (Forget al., 1999; Madeleine et al., 2011; Millour et al., 2018; Montabone et al., 2020). We still notice a good correlation between our cap edges and the simulations. A gap in the detections is present between $L_S \sim 190°$ and $\sim 215°$, resulting from the interruption of nadir acquisitions using the orders 190, 169, 168 and 167 during this period. As shown in Fig. 7A, only MY35 and MY36 cover this period, presenting a correlation in the cap boundaries results.

It is known that the global dust storm has an effect on the sublimation phase of the south polar cap (Piqueux et al., 2015; Calvin et al., 2017). Similarities have been observed between the two global dust storms occurring in MY25 and MY34 (Wolkenberg et al., 2020). They encircle the entire planet at a similar season ($L_S \sim 190°$), although the MY34 storm is characterised by a shorter decay phase compared to the one in MY25. During this season, the southern latitudes are more exposed to the Sun than northern latitudes. Due to high dust opacity, the heating rate of the atmosphere is enhanced (Guzewich et al., 2019; Kass et al., 2020; López Valverde et al., 2022). Wolkenberg et al. (2020) observed a clear trend of atmospheric temperatures with dust. On the other hand, atmospheric dust inhibits the solar radiation from reaching the lower atmospheric layers, and hence the surface (Wolkenberg et al., 2018). Therefore, surface temperature tends to decrease during the day. The more dust in the atmosphere, the more the surface is cooling during the day (Streeter et al., 2020). An opposite effect occurs during the night. Indeed, a surface and near-surface warming effect is observed due to increased long-wave emission and backscattering from the increased aerosol and resulting higher atmospheric temperatures (Martínez et al., 2017; Guzewich et al., 2019). Higher dust opacity and higher surface temperatures at night have been observed in MY34 compared to MY25 (Wolkenberg et al., 2020). Moreover, nightside warming in MY34 was more important and persistent over time than diurnal cooling, allowing to counterbalance the dayside cooling. It resulted an effect of surface warming in diurnally averaged surface temperature (Streeter et al., 2020). In the southern polar region, Mars Climate Sounder observed a large amount of dust over the polar cap (Kleinböhl et al., 2020). The atmosphere and its near surface layers progressively warmed, reaching a temperature of 200 K from $L_S \sim 190°$ to ~235°, with a peak of ~230 K at L_S 215°-220° (~130 K–150 K before the global dust storm).

Based on the above discussion, an acceleration of the recession of the

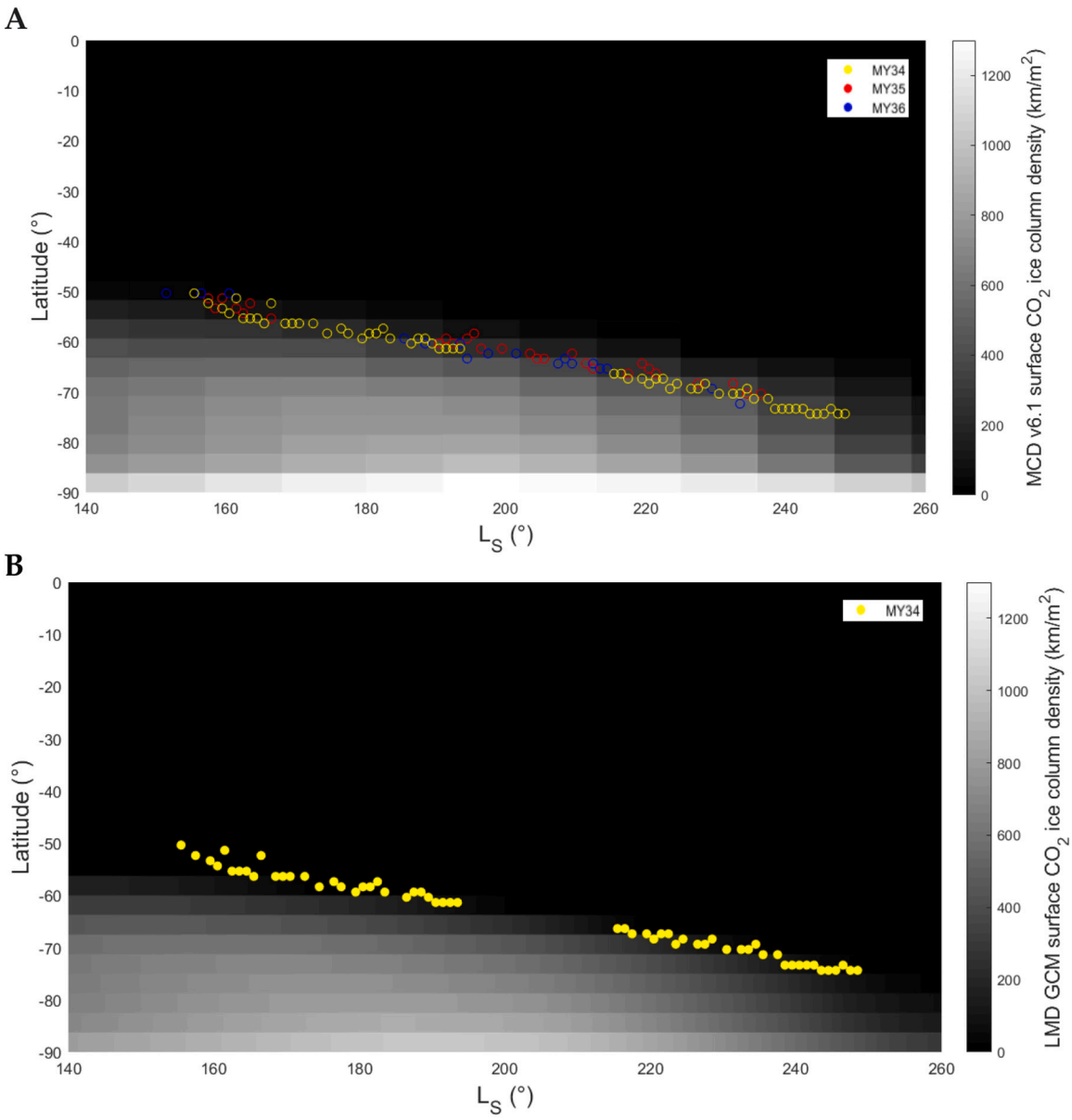

Fig. 7. Polar cap edges estimated from the latitudinal trend of the NII. (A) Comparison between our cap boundaries estimation for MY34–36 and the MCD v6.1 CO_2 ice column density predictions. (B) Comparison between our cap boundaries definition for MY34 and LMD GCM simulations using MY34 dust activity.

cap should be observed in MY34 compared to MY35 and 36. Nevertheless, the limited temporal coverage during the global dust storm in MY34 (yellow points in Fig. 7A) complicates the comparison between the three Martian Years. Moreover, such a comparison must be carried out on a homogeneous spatial coverage between years. To do this, NOMAD has to provide more data in order to reach a significant number of observations of the cap. For these reasons, the current data set does not allow us to investigate the possible effects of dust storms on the Southern polar cap.

5.2. Polar projection

In this section, we discuss the southern sublimation phase during early and mid-spring for MY34–36 (data are binned 1° by 1° of longitude and latitude) by studying the polar projections of NII and BD2292 in 4 periods of time, L_S = 180°-190°, L_S = 200°-210°, L_S = 220°-230° and L_S = 240°-250°. Due to the specific TGO orbit, LNO observations are acquired up to latitudes 75°S. Therefore, the retreat of the cap can be observed until $L_S \sim 250°$. After that period, the polar cap no longer extends to these latitudes (Langevin et al., 2007; Brown et al., 2010). The results are presented in Fig. 8. Left panels show the NII (see Section 4.1), middle panels the BD2292 (see Section 4.2), and the right panels present the latitudinal trend of the BD2292. As already mentioned (see Section 2), the main objective of NOMAD is the analysis of trace gases and, hence, the spatial coverage is not optimised for surface analysis. Nevertheless, thanks to the NII and BD2292, it is possible to partially distinguish the seasonal variations along the LNO ground tracks during the presublimation and the cryptic phases (Brown et al., 2010).

Fig. 8A shows the presublimation phase. During this period, the seasonal cap clearly extends equatorward of 60°S (see left panel). Similarly to Fig. 6, we study the latitudinal trend of the BD2292, in which the values suddenly increase at latitude 56°S (see right panel). This indicates the presence of the seasonal cap, which is symmetrical and characterised by low and homogenous albedo presenting strong CO_2 ice signatures (see left and middle panels) (Langevin et al., 2007).

The cryptic phase is observed in Fig. 8B and C. The low albedo cryptic region is localised between longitudes 60°E and 150°W (i.e. 60°E and 210°E) and below latitude 70°S. It has been identified as a region in

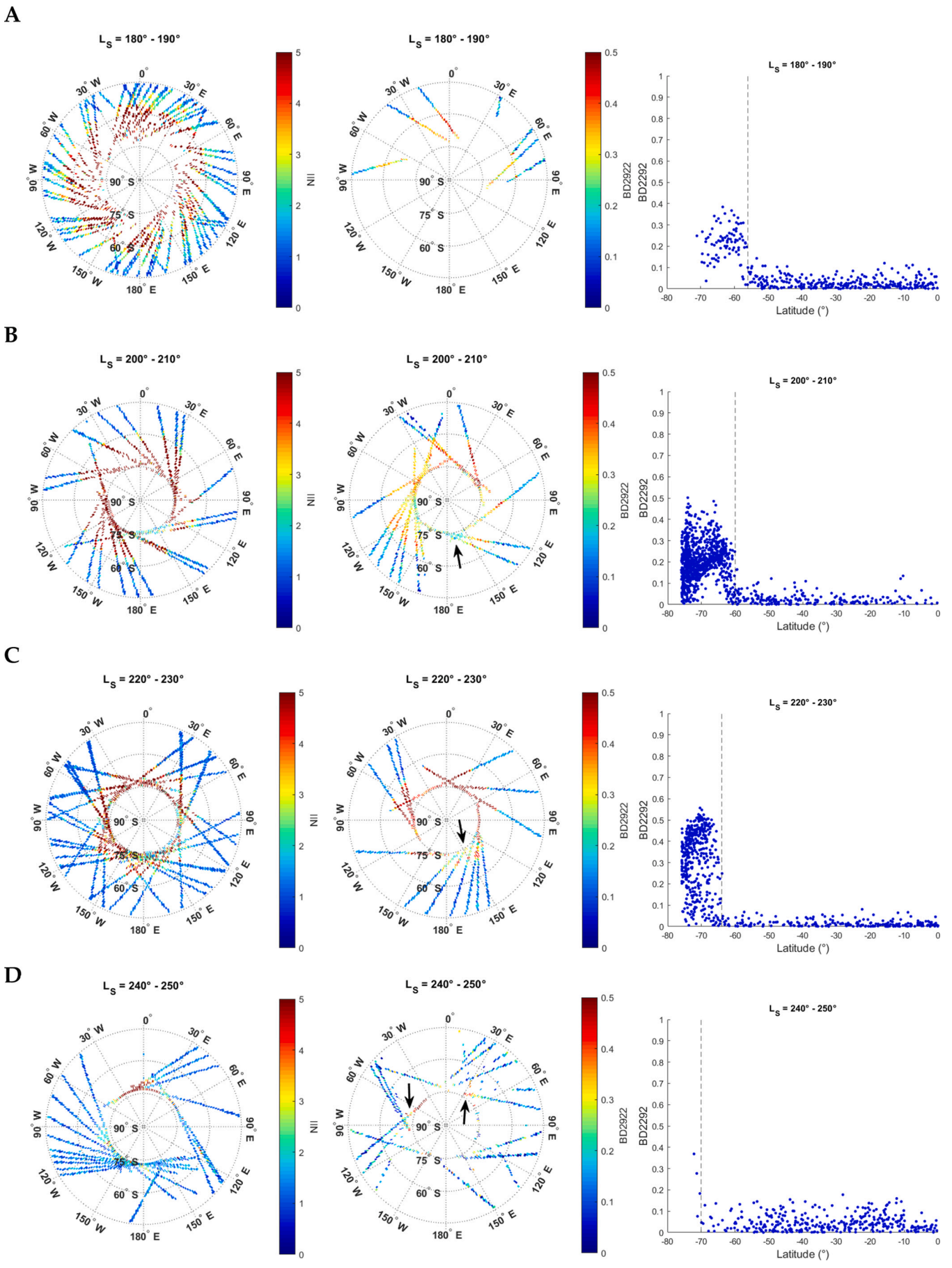

(caption on next page)

Fig. 8. (A) South polar projections of NII (left) and BD2292 (middle) for the period of L_S = 180° - 190° in MY34–36 binned 1° by 1°. The colour bars have been saturated in order to emphasise the colour dynamic. The lower values (blue tint) correspond to ice-free regions. The BD2292 profiles over the probed latitudes helps in the visualisation of the retreat of the cap (right). The vertical dashed black line indicates the latitude in which the BD2292 values increase suddenly due to the presence of CO_2 ice. (B) Same for the period of L_S = 200° - 210°. (C) Same for the period of L_S = 220° - 230°. (D) Same for the period of L_S = 240° - 250°. (For interpretation of the references to colour in this figure legend, the reader is referred to the web version of this article.)

which the CO_2 ice slab is contaminated by dust (Kieffer et al., 2000; Langevin et al., 2007). As we can see in the middle panel in Fig. 8B and C (see black arrow), the probed parts of the cryptic region (between longitudes 150°E and 150°W, i.e. 150°E to 210°E, and around latitude 75°S) present lower BD2292 values, with respect to the other parts of the cap, due to the possible dust contamination (see Fig. 4C). Regarding the NII (see left panel in Fig. 8B), we also notice lower values in the cryptic region, which should confirm the presence of high dust abundance (Oliva et al., 2022). On the other hand, the change in the NII values for this region is not so evident in Fig. 8C. This can be explained by the presence of water ice inside the cryptic region during this period (Brown et al., 2010), which can counterbalance the effects of dust on the NII. Regarding the retreat of the cap (see right panels), the seasonal cap extends below latitudes 60°S, where a very high albedo characterises its outer regions (Kieffer et al., 2000; Langevin et al., 2007; Schmidt et al., 2009).

The last period partially covered by NOMAD is the asymmetrical retreat of the seasonal cap. During this period, the seasonal cap completely disappears in latitudes above 75°S between longitudes 60°E and 150°W (i.e. 60°E to 210°E) (Langevin et al., 2007). Both NII and BD2292 present a scarce surface coverage in Fig. 8D. Nevertheless, we can see that the seasonal cap is present in latitudes above 75°S between longitudes 90°W and 60°E (see black arrows in middle panel). This is consistent with OMEGA and CRISM observations, which have identified these bright albedo regions defined by strong CO_2 ice signatures (Langevin et al., 2007; Schmidt et al., 2009; Brown et al., 2010).

5.3. CO_2 ice thickness

The high spectral resolution of NOMAD offers the possibility to retrieve some CO_2 ice properties. Nevertheless, the main difficulty remains in the acquisition of LNO observations through the different orders, hence impacting the spectral and spatial coverages. Moreover, the instrumental characteristics are not fully ideal for surface spectroscopy (see Section 2). Therefore, in this section, we adopt a semi-qualitative approach to discuss the possibility to reproduce the 2.29 μm CO_2 ice absorption band (order 193) using the Planetary Spectrum Generator (PSG) model (Villanueva et al., 2018). We attempt to estimate the "equivalent grain size" (henceforth called grain size), which is defined as the mean distance between two scattering interfaces within the CO_2 ice (Langevin et al., 2007). This is defined as the "CO_2 ice thickness" in the PSG model.

5.3.1. PSG model

The PSG model is an online tool dedicated to the synthesis and retrieval of planetary spectra (atmospheres and surfaces) for a broad range of wavelengths (0.5 μm to 100 mm) from any observatory (ground based telescope, orbiter or lander). PSG also permits to synthesise/retrieve mass-spectrometry data of orbiters, landers and laboratory instrumentation. It combines several state-of-the-art radiative transfer models, spectroscopic databases and planetary databases (i.e., climatological and orbital). This tool is hence suitable for the analysis of the NOMAD observations (Liuzzi et al., 2020). For the first time, PSG is used in a frame of a surface ice analysis with the LNO data in order to estimate the CO_2 ice equivalent grain size, i.e. the CO_2 ice thickness. In this work, we consider the Lambert (isotropic scattering) model for simulating the absorbed light at a surface, taking into account the LNO observing geometry. Regarding the surface composition, the model includes >20,000 species. We use the CO_2 ice optical constant from the NASA Goddard Space Flight Center (GSFC) (Gerakines and Hudson, 2020). The retrievals are performed on LNO observations acquired over regions where clean CO_2 ice slabs are expected. For that reason, we do not include H_2O ice optical constant in the surface composition. Nevertheless, for any dust impurities on the CO_2 ice, we rely on the optical constant from the Air Force Cambridge Research Labs (AFCRL) (Harris and Rowan-Robinson, 1977). PSG is also able to perform multiple scattering from atmospheric aerosols by using the discrete ordinate method (Stamnes et al., 2017). Therefore, for suspended dust, we use the refractive indices derived with CRISM observations (Wolff et al., 2009). The model assumes a thermal structure of the Martian atmosphere coming from the MCD climatology predictions (Millour et al., 2018). During the retrievals, it employs the Optimal Estimation Method (Rodgers, 2000), which analyses each spectrum individually through a Gauss-Newton iterative approach. More details about the PSG model and the retrievals method can be found in Villanueva et al. (2018) and Liuzzi et al. (2020).

5.3.2. Errors estimation

In order to perform the retrievals with PSG, the AOTF and Blaze functions convolution are applied to the synthetic spectra. Indeed, as already mentioned in Section 2, the general shape of the LNO spectra is affected by the AOTF transmission (defined as the sum of a sinc squared and a Gaussian function) and by the Blaze function (defined as a sinc squared function). It is important to mention that the sinc squared AOTF function allows some photons from adjacent diffraction orders to reach the detector (Liuzzi et al., 2019). This complexity hence challenges the AOTF definition for the LNO channel, impacting the uncertainty on the LNO spectra. In addition to these instrumental errors, the SNR also depends on the radiation entering the spectrometer, and so observational parameters such as SZA, surface albedo, etc. can affect it (see Section 2 and 3).

In this section, we adopt an independent manner in order to estimate the total uncertainties, i.e. the instrumental and observational errors, associated with the spectra and to analyse the source of variability. To do so, we select all the spectra falling in a dayside equatorial region of 10° latitude by 10° longitude for MY35–36 (>100), for which we assume that no surface CO_2 ice is present. As the SZA strongly impacts the SNR, the sample spectra are divided in 10° SZA intervals, ranging from SZA = 20° to 75°. Moreover, we normalise each spectrum with the signal intensity at the middle of the order. This is done in order to mitigate eventual surface albedo and aerosols variations that would mostly affect the radiometric signal of the considered observations. Then, we compute, for each SZA interval, an averaged intensity value for each wavelength and estimate the standard deviation. As an example, Fig. 9A shows the averaged spectrum (in blue) for SZA = 40° - 50° in MY35–36. We can see that the spectrum is modulated, especially at the edges, whereas normally we should obtain a normalised continuum spectrum around 1 (as we assume the absence of surface CO_2 ice in a dayside equatorial region). In fact, the modulation in the spectrum is the result of the AOTF function. We estimate an averaged standard deviation of 20% for all wavelengths. As we can see in Fig. 9B, it increases from the middle of the order to its edges. The standard deviation ranges from 4% to 9% between 2288 nm and 2298 nm, while it is larger than 100% at 2305 nm due to a reduced blaze efficiency at this edge of the detector. This difference in uncertainty value in the order suggests that the dominant source of variability results from the instrumental effects (instrumental noise, the AOTF and Blaze functions). From this analysis, we can hence provide an estimation of the error associated with the spectra

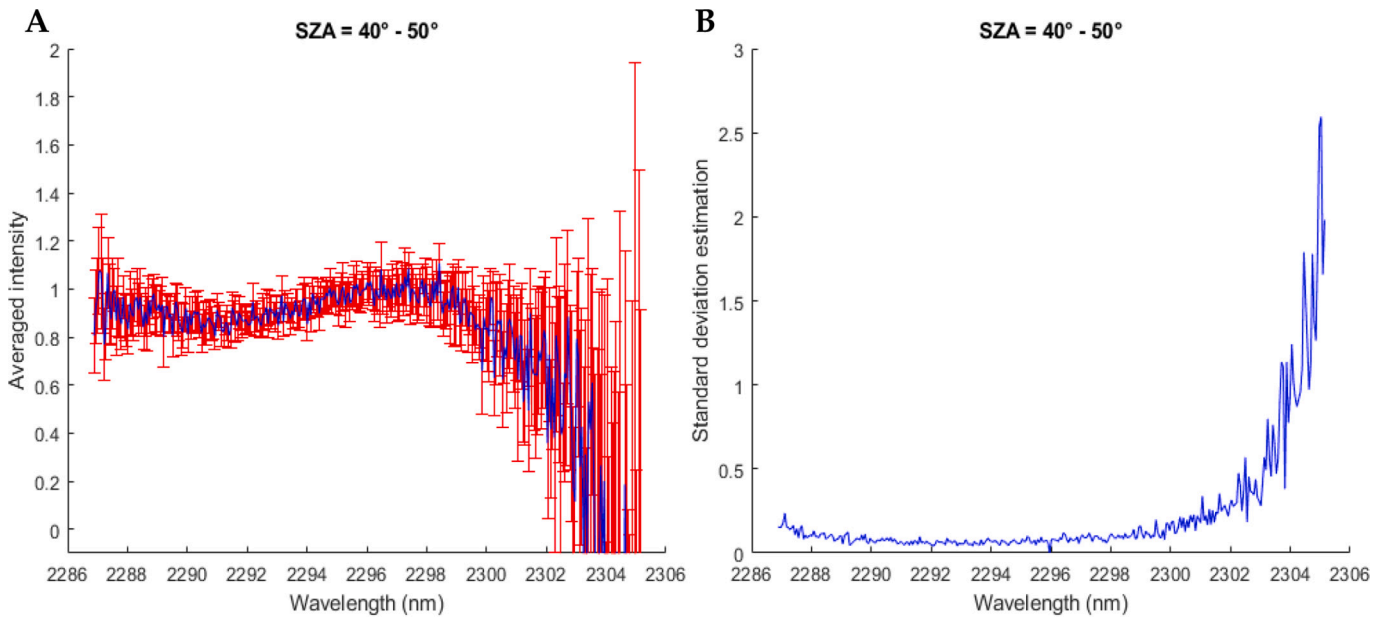

Fig. 9. (A) Averaged spectrum (in blue) of an equatorial region for SZA = 40° - 50° in MY35–36. For each wavelength, the standard deviation is computed given the error bars estimation in red. (B) Variation of the standard deviation values, ranging from 4% in the middle of the order to >100% at 2305 nm. (For interpretation of the references to colour in this figure legend, the reader is referred to the web version of this article.)

(instrumental and observations uncertainties) to the PSG model.

5.3.3. *Equivalent grain size estimation*

For this exercise, we select some spectra of the south polar regions with the lowest SZA and where a strong CO_2 ice signature is expected during the presublimation (see Fig. 8A) and the cryptic phases (see Fig. 8B and C).

Table 1 shows spatial and physical parameters related to some examples of observations registered during these two different periods (2 in the presublimation phase and 3 in the cryptic phase). As already mentioned in Section 5.2, low and homogenous albedo characterises the CO_2 ice seasonal cap during the presublimation phase. We observe surface albedo around 0.1–0.15 with a BD2292 estimation around 0.4–0.5. Such spectra acquired over the seasonal cap can be interpreted as a clean CO_2 ice slab with a grain size of tens of centimetres (20 cm – 50 cm). They are observed over a large range of longitudes, except at the edges of the cap (Langevin et al., 2007). The PSG tool is able to model the selected spectrum by estimating a grain size of ~27 cm (see line 1 in Table 1). At the cap edge, i.e. close to the sublimating frost, we obtain grain sizes of ~12 cm (see line 2 in Table 1). This suggests that the grain size decreases with time as the ice sublimes, which has been also observed by TES and CRISM (Kieffer et al., 2000; Brown et al., 2010; Andrieu et al., 2018).

Regarding the cryptic phase, spectra are characterised by relatively high albedo. We observe values of 0.4–0.5, while Langevin et al. (2007) reported albedo values of 0.7 using OMEGA observations. They found grain sizes of 5–10 cm at the outer regions. Fig. 10 presents the PSG fit obtained for a LNO spectrum over the outer regions of the cap. The model reproduces the data by estimating a grain size of ~8 cm (see line 3 in Table 1), hence consistent with OMEGA observations (Langevin et al., 2007). The two last observations listed in Table 1 are acquired close to the so-called Mountains of Michel area (around latitudes 70°S +/− 3° and longitudes 35°W +/− 5°), defined as a bright albedo region (James et al., 1987; Smith et al., 1999; Kieffer et al., 2000; Langevin et al., 2007; Brown et al., 2010). The retrievals return grain sizes of ~15 cm and ~ 12 cm. This range of values is quite consistent with the order of magnitude found by Langevin et al. (2007) (grain size at outer bright region ~5–10 cm) and Andrieu et al. (2018), but not with TES

Table 1
Orbits, L_S, latitudes, longitudes, SZA, equivalent grain size estimations with PSG, goodness of the fit and comparison with previous studies are listed for some selected LNO spectra during the presublimation and cryptic phases.

Phase	Orbit	L_S (°)	Latitude (°)	Longitude (°)	SZA (°)	Grain size (cm)	Reduced χ^2	Literature
Presubl.	20220310_070842	187.8	58.2 S	9.9 W	65.5	27 +/− 3.8	0.13	20 cm - 50 cm (Langevin et al., 2007) 80 cm (Andrieu et al., 2018)
Presubl.	20200504_083128	194.8	61.9 S	57.6 W	66.2	12 +/− 1	0.60	12 cm - 15 cm (Calvin and Martin, 1994); ~ 10 cm (Kieffer et al., 2000) 6 cm - 8 cm (Brown et al., 2010) 40 cm (Andrieu et al., 2018)
Cryptic	20200527_090659	208.6	66.2 S	95.1 E	56.8	8 +/− 0.8	0.15	5 cm - 10 cm (Langevin et al., 2007) 2 cm - 3 cm (Brown et al., 2010) 30 cm (Andrieu et al., 2018)
Cryptic	20220508_203944	223.7	68.1 S	53.8 W	52.4	15 +/− 0.8	0.40	>1 cm (Kieffer et al., 2000); 5 cm - 10 cm (Langevin et al., 2007) 20 cm (Andrieu et al., 2018)
Cryptic	20220524_021241	233.2	67.4 S	34.2 W	62.2	12 +/− 1.5	0.66	> 1 cm (Kieffer et al., 2000); 5 cm - 10 cm (Langevin et al., 2007) 10 cm (Andrieu et al., 2018)

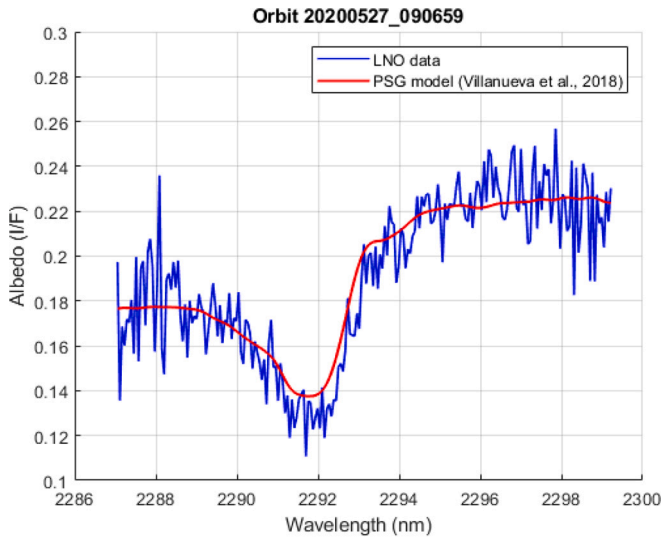

Fig. 10. PSG fit on the 2.29 μm CO_2 ice absorption band well present in the LNO spectrum (orbit 20200527_090659). A reduced χ^2 of 0.15 is obtained. See line 3 in Table 1 for more details.

observations. Indeed, Kieffer et al. (2000) suggested fine grains of a 100 μm radius. On the other hand, under low atmospheric dust abundance (dust mass mixing ratio $< 10^{-4}$ kg/kg), they have observed grain sizes much larger than 1 cm. Therefore, we use the MCD v6.1 predictions in order to estimate the suspended dust content for the last observation in Table 1, which is the closest to the Mountains of Michel. The model returns a dust mass mixing ratio of 4.1×10^{-6} kg/kg, which means that the order of magnitude of grain size (in centimetre) is in agreement with TES observations.

Regarding Andrieu et al. (2018), they estimated the full sublimation phase in the Richardson crater (at longitude 180°W and latitude 72°S) outside a dark spot. They found a global decrease in the CO_2 ice slab thickness from 40 cm at $L_S = 197°$ to 1 cm at $L_S = 250°$, taking inclusions and aerosols into account. Even though the global trend is in agreement with our study, the value can be different by a factor of 3 (see lines 1 to 3 in Table 1). This may be due to the radiative transfer assumptions and/or the difference in spatial scale and localisation between our study and that of Andrieu et al. (2018).

The errors of the retrieved parameters in Table 1 have been estimated by a statistical approach (bootstrapping procedure; Efron and Tibshirani, 1994). We use the measurement errors to create randomised spectra within the error bars of the nominal one. Each iteration provides a randomised spectrum that follows the same statistical characteristics as the real observations. Then, we perform the retrieval for a statistically significant number of times. Therefore, the distribution of the retrieved parameter values can be analysed to estimate the associated errors. It is important to mention that we do not attempt to analyse in-depth the 2.29 μm feature. A more robust quantitative modelling would require to take into account several physical parameters and a complete estimation of the retrieved parameters errors. This is beyond the scope of this work. As already mentioned, we analyse the possibility to reproduce the 2.29 μm absorption band by adopting a semi-qualitative approach in order to provide the order of magnitude of the grain size. As shown in Table 1, the PSG model is able to reproduce correctly the LNO spectra. The obtained results are in good agreement with the order of magnitude of the grain size estimation of previous studies (Calvin and Martin, 1994; Kieffer et al., 2000; Langevin et al., 2007; Brown et al., 2010; Andrieu et al., 2018). To conclude, this section shows that the PSG model is suitable for a surface CO_2 ice analysis through the order 193.

6. Conclusion

Even if devoted to trace gases in the Martian atmosphere, NOMAD has also proven to be a suitable spectrometer to study surface CO_2 ice of Mars at high resolution using the LNO nadir IR channel (Oliva et al., 2022), despite the instrumental features (see Section 2). In this work, we have further explored the LNO dataset information content. We have defined an updated method using the three diffraction orders (orders 167, 168, 169) located on the short wavelength shoulder of the 2.7 μm ice absorption band in order to map surface ice by considering the best spatial coverage. The method is based on spectral ratio capable of detecting surface albedo variations related to ice (New Ice Index, see Section 4.1). Moreover, we have also investigated CO_2 ice by defining a pseudo-band depth for NOMAD (BD2292, see Section 4.2) through the 2.29 μm absorption band (order 193). We applied both spectral parameters on the LNO dataset from MY34 ($L_S = 150°$) to MY36 ($L_S = 360°$) and constructed latitudinal-seasonal maps for surface ice detection. It represents the highest spatial coverage to date of these observations. We focused specifically on the Southern polar cap to analyse the seasonal and potential interannual changes over MY34–36 (see Section 5.1 and 5.2). To do that, we have estimated the polar cap edges based on the latitudinal trend of the spectral parameters. Our polar cap edges definition is consistent with the MCD v6.1 (Forget et al., 1999; Millour et al., 2018) and LMD GCM CO_2 ice column predictions (Forget al., 1999; Madeleine et al., 2011; Millour et al., 2018; Montabone et al., 2020). Globally, seasonal changes seem repeatable for MY34–36 (see Section 5.1). Finally, we discussed the potential for using the 2.29 μm absorption band to retrieve information about CO_2 ice grain size by adopting a semi-qualitative approach. We used the Planetary Spectrum Generator tool (Villanueva et al., 2018) on observations where a clean and thick CO_2 ice slab is expected (see Section 5.3). The results obtained for the presublimation and cryptic phases are in the order of centimetres, which is consistent with previous studies (Calvin and Martin, 1994; Kieffer et al., 2000; Langevin et al., 2007; Brown et al., 2010; Andrieu et al., 2018) (see Section 5.3.3).

Continuous observations enhance our understanding of the Martian surface ice. The results presented in this work (see Section 5) appear to be consistent with previous studies (e.g. using OMEGA, CRISM, TES data). They confirm and help in refining our current knowledge of the Southern polar cap, through observation of the sublimation process. Additionally, order 193 appears to be a good candidate for the CO_2 ice identification, opening further perspectives for the analysis of Martian ice deposits. Indeed, the use of the PSG model reveals its highly sensitivity to the microphysical properties of the ice. This indicates the large potential for more detailed exploitation of this order, e.g. for the analysis of small ice crystals. A dedicated radiative transfer model will allow to analyse in depth CO_2 ice at a higher resolution. This will provide significant insights of the microphysical properties of the ice, complementing the results of previous studies (see Table 1 in Section 5.3.3). As it was done with order 189 in Oliva et al. (2022), another possible perspective with order 193 is the CO_2 ice cloud detection, which can provide additional information on their distribution, seasonality and microphysical properties.

Finally, this paper represents one of several studies dedicated to the exploitation of the LNO nadir dataset and opens the way for different follow-up papers. As a direct continuation to this work, an in-depth radiative transfer analysis of the 2.29 μm feature in CO_2 ice is already planned. Regarding the cloud analysis (Oliva et al., 2022; Ruiz Lozano et al., 2022), further comparison with the NOMAD-UVIS channel about cloud detection is currently being performed.

Funding

The NOMAD experiment is led by the Royal Belgian Institute for Space Aeronomy (IASB-BIRA), assisted by Co-PI teams from Spain (IAA-CSIC), Italy (INAF-IAPS), and the United Kingdom (Open University).

This project was funded by the Belgian Science Policy Office (BELSPO), with the financial and contractual coordination by the ESA Prodex Office (PEA 4000103401,4000121493), by the Spanish Ministry of Science and Innovation (MCIU) and by European funds under grants PGC2018-101836-B-I00 ESP2017-87143-R (MINECO/FEDER), as well as by the UK Space Agency through grants ST/V002295/1, ST/V005332/1, ST/X006549/1, ST/Y000234/1 and ST/S00145X/1 and the Italian Space Agency through grant 2018-2-HH.0. US investigators were supported by the National Aeronautics and Space Administration. Canadian investigators were supported by the Canadian Space Agency.

Author contributions

Conceptualization, L.R.L., F.O. and G.B.; Methodology, L.R.L., F.O., G.B., F.S., G.C.M., and Ö.K.; Software, L.R.L.; Validation, L.R.L., F.O., G. B., and Ö.K.; Formal Analysis, L.R.L. and F.O.; Investigation, L.R.L., F.O. and G.B.; Resources, L.R.L., G.B., F.O., I.R.T. and B.R.; Data Curation, L. R.L., G.B., F.O., I.R.T., and B.R.; Writing—Original Draft Preparation, L. R.L.;Writing—Review & Editing, L.R.L., F.O.,G.B., Ö.K., V.D., E.D., F.G. C., I.R.T., F.S., G.C.M. and M.R.P.; Supervision, Ö.K., V.D., G.B., A.C.V., F.D., B.R. and M.R.P.; Project Administration, Ö.K., V.D., G.B., A.C.V.,M. R.P. and J.J.L.M.; Funding Acquisition, L.R.L., Ö.K., G.B., A.C.V.,M.R.P. and J.J.L.M.

Declaration of Competing Interest

The authors declare no conflict of interest.

Data availability

The data used for this study was obtained from the Royal Belgian Institute for Space Aeronomy (IASB-BIRA). At the time of writing, the dataset is not publicly available, however the LNO data used for this study will be added to the ESA Planetary Science Archive (https://archives.esac.esa.int/psa) in the near future.

Acknowledgments

This work was also supported by the Belgian Fonds de la Recherche Scientifique–FNRS under grant number EOS-30442502. F. S. and G. C. M. would like to thank support from the “Institut National des Sciences de l’Univers” (INSU), the “Centre National de la Recherche Scientifique” (CNRS) and “Centre National d’Etudes Spatiales” (CNES) through the “Programme National de Planétologie”. J.J.L.M. acknowledges financial support from the State Agency for Research of the Spanish MCIU through the ‘Center of Excellence Severo Ochoa’ award for the Instituto de Astrofísica de Andalucía (SEV-2017-0709) and by grant PGC2018-101836-B-100 funded by MCIU/AEI/10.13039/501100011033 and by “ERDF A way of making Europe”. M.R.P acknowledges funding from the UK Space Agency through grants ST/V002295/1, ST/V005332/1, ST/X006549/1, and ST/Y000234/1.

References

Andrieu, F., Schmidt, F., Douté, S., Chassefière, E., 2018. Ice state evolution during spring in Richardson crater, Mars. Icarus 315, 158–173. https://doi.org/10.1016/j.icarus.2018.06.019.

Appéré, T., Schmitt, B., Langevin, Y., Douté, S., Pommerol, A., Forget, F.,. and Bibring, J.-P. (2011). Winter and spring evolution of northern seasonal deposits on Mars from OMEGA on Mars Express. J. Geophys. Res. Planets, 116 (E5). Retrieved from https://agupubs.onlinelibrary.wiley.com/ doi/abs/10.1029/2010JE003762 doi: 10.1029/2010JE003762.

Bell, J.F., et al., 2000. Mineralogic and compositional properties of Martian soil and dust: Results from Mars pathfinder. J. Geophys. Res. 105, 1721–1755.

Bell, J.F., et al., 2009. Mars reconnaissance orbiter Mars color imager (MARCI): instrument description, calibration, and performance. J. Geophys. Res. 114, E08S92. https://doi.org/10.1029/2008JE003315.

Benson, J.L., James, P.B., 2005. Yearly comparisons of the martian polar caps: 1999–2003 Mars orbiter camera observations. Icarus 174 (2), 513–523. ISSN 0019-1035,. https://doi.org/10.1016/j.icarus.2004.08.025. ISSN 0019-1035,.

Benson, J.L., Kass, D.M., Kleinböhl, A., McCleese, D.J., Schofield, J.T., Taylor, F.W., 2010. Mars’ south polar hood as observed by the Mars Climate Sounder. J. Geophys. Res. Planets 115.

Bibring, J.P., Soufflot, A., Berthé, M., Langevin, Y., Gondet, B., Drossart, P., Buoyé, M., Combes, M., Puget, P., Semery, A., et al., 2004a. OMEGA: Observatoire Pour La Minéralogie, l’Eau, Les Glaces et l’Activité. In: Wilson, A., Chicarro, A. (Eds.), Mars Express: The Scientific Payload, 1240. European Space Agency, Paris, France, pp. 37–49.

Bernard-Michel, C., Douté, S., Fauvel, M., Gardes, L., Girard, S., 2009. Retrieval of Mars surface physical properties from OMEGA hyperspectral images using regularized sliced inverse regression. J. Geophys. Res. 114, E06005 https://doi.org/10.1029/2008JE003171.

Bibring, J.-P., et al., 2004b. Perennial water ice identified in the south polar cap of Mars. Nature 428, 627–630.

Bibring, J.-P., Langevin, Y., Gendrin, A., Gondet, B., Poulet, F., Berthé, M., the OMEGA team, 2005. Mars surface diversity as revealed by the OMEGA/Mars Express observations. Science 307 (5715), 1576–1581 doi: 523 10.1126/science.1108806.

Brown, A.J., Calvin, W.M., McGuire, P.C., Murchie, S.L., 2010. Compact reconnaissance imaging spectrometer for Mars (CRISM) south polar mapping: first Mars year of observations. J. Geophys. Res. 115, E00D13 https://doi.org/10.1029/2009JE003333.

Brown, A.J., Calvin, W.M., Murchie, S.L., 2012. Compact reconnaissance imaging spectrometer for Mars (CRISM) north polar springtime recession mapping: first 3 Mars years of observations. J. Geophys. Res. 117, E00J20 https://doi.org/10.1029/2012JE004113.

Brown, A.J., Piqueux, S., Titus, T.N., 2014. Interannual observations and quantification of summertime H_2O ice deposition on the Martian CO_2 ice south polar cap. Earth Planet. Sci. Lett. 406, 102–109. ISSN 0012-821X,. https://doi.org/10.1016/j.epsl.2014.08.039. ISSN 0012-821X,.

Calvin, W.M., Martin, T.Z., 1994. Spatial variability in the seasonal south polar cap of Mars. J. Geophys. Res. 99 (E10), 21143. https://doi.org/10.1029/94je02011.

Calvin, W.M., Cantor, B.A., James, P.B., 2017. Interannual and seasonal changes in the south seasonal polar cap of Mars: observations from MY 28-31 using MARCI. Icarus 292, 144–153. ISSN 0019-1035,. https://doi.org/10.1016/j.icarus.2017.01.010. ISSN 0019-1035,.

Cazenave, A., Balmino, G., 1981. Meteorological effects on the seasonal variations on the rotation of Mars. Geophys. Res. Lett. 8 (3), 245–248.

Christensen, P.R., Bandfield, J.L., Hamilton, V.E., Ruff, S.W., Kieffer, H.H., Titus, T.N., Malin, M.C., Morris, R.V., Lane, M.D., Clark, R.L., et al., 2001. Mars global surveyor thermal emission spectrometer experiment: investigation description and surface science results. J. Geophys. Res. Planets 106, 23823–23872.

Christensen, P.R., Jakosky, B.M., Kieffer, H.H., Malin, M.C., McSween Jr., H.Y., Nealson, K., Mehall, G.L., Silverman, S.H., Ferry, S., Caplinger, M., Ravine, M., 2004. The thermal emission imaging system (THEMIS) for the Mars 2001 odyssey Mission. Space Sci. Rev. 110, 85–130.

Clancy, R.T., Wolff, M.J., Whitney, B.A., Cantor, B.A., Smith, M.D., 2007. Mars equatorial mesospheric clouds: global occurrence and physical properties from Mars Global Surveyor Thermal Emission Spectrometer andMars Orbiter Camera limb observations. J. Geophys. Res. (Planets) 112 (E4), E04004.

Clark, R.N., Roush, T.L., 1984. Reflectance spectroscopy: quantitative analysis techniques for remote sensing applications. J. Geophys. Res. 89, 6329–6340.

Cruz Mermy, G., Schmidt, F., Thomas, I.R., Daerden, F., Ristic, B., Patel, M.R., Lopez-Moreno, J.J., Bellucci, G., Vandaele, A.C., 2022. Calibration of NOMAD on ExoMars trace gas orbiter: part 3—LNO validation and instrument stability. Planet. Space Sci. 218, 105399.

Cull, S., Arvidson, R.E., Mellon, M., Wiseman, S., Clark, R., Titus, T., Morris, R.V., McGuire, P., 2010. Seasonal H2O and CO2 ice cycles at the Mars Phoenix landing site: 1. Prelanding CRISM and HiRISE observations. J. Geophys. Res. 115, E00D16.

Defraigne, P., de Viron, O., Dehant, V., Van Hoolst, T., Hourdin, F., 2000. Mars rotation variations induced by atmospheric CO2 and winds. J. Geophys. Res. (Planets) 105 (E10), 24563–24570.

Dehant, V., Le Maistre, S., Baland, R.-M., Bergeot, N., Karatekin, Ö., Péters, M.-J., Rivoldini, A., Ruiz Lozano, L., Temel, O., Van Hoolst, T., Yseboodt, M., Mitrovic, M., Kosov, A.S., Valenta, V., Thomassen, L., Karki, S., Al Khalifeh, K., Craeye, C., Gurvits, L.I., Marty, J.-C., Asmar, S.W., Folkner, W.M., 2020. The radioscience LaRa instrument onboard ExoMars 2020 to investigate the rotation and interior of mars. Planet. Space Sci. 180, 104776. ISSN 0032–0633. https://doi.org/10.1016/j.pss.2019.104776. ISSN 0032–0633.

Dollfus, A., 1973. New optical measurements of planetary diameters IV. Size of the north polar cap of Mars. Icarus 18 (1), 142–155. ISSN 0019-1035,. https://doi.org/10.1016/0019-1035(73)90181-4.

Efron, B., Tibshirani, R.J., 1994. An Introduction to the Bootstrap, 1st ed. Chapman and Hall/CRC. https://doi.org/10.1201/9780429246593.

Fischbacher, G.E., Martin, L.J., Baum, W.A., 1969. Martian polar cap boundaries. In: Final Report, Part A, Contract 951547, Jet Propulsion Laboratory, Pasadena, CA. Planetary Research Center, Lowell Observatory Flagstaff, AZ.

Forget, F., Hourdin, F., Fournier, R., Hourdin, C., Talagrand, O., Collins, M., 1999. Improved general circulation models of the Martian atmosphere from the surface to above 80 km. J. Geophys. Res. 104, 24155–24175.

Formisano, V., Angrilli, F., Arnold, G., Atreya, S., Bianchini, G., Biondi, D., et al., 2005. The planetary Fourier spectrometer (PFS) onboard the European Mars express mission. Planet. Space Sci. 53 (10), 963–974. https://doi.org/10.1016/j.pss.2004.12.006.

Formisano, V., Maturilli, A., Giuranna, M., D'Aversa, E., Lopez-Valverde, M.A., 2006. Observations of non-LTE emission at 4 5 microns with the planetary Fourier spectrometer aboard the. Mars Exp. Mission. 182 (1), 51–67.
Gendrin, A., et al., 2005. Sulfates in Martian layered terrains: the OMEGA/Mars express view. Science 307, 1587–1591.
Gerakines, P.A., Hudson, R.L., 2020. A Modified Algorithm and Open-source Computational Package for the Determination of Infrared Optical Constants Relevant to Astrophysics. Astrophys. J. 901 (1), 52. https://doi.org/10.3847/1538-4357/abad39.
Gillespie, H.E., Greybush, S.J., Wilson, R.J., 2020. An investigation of the encirclement of Mars by dust in the 2018 global dust storm using EMARS. J. Geophys. Res. Planets 125, e2019JE006106. https://doi.org/10.1029/2019JE006106.
Guzewich, S.D., Lemmon, M., Smith, C.L., Martínez, G., de Vicente-Retortillo, Á., Newman, C.E., et al., 2019. Mars science laboratory observations of the 2018/Mars year 34 global dust storm. Geophys. Res. Lett. 46, 71–79. https://doi.org/10.1029/2018GL080839.
Hansen, G.B., 2005. Ultraviolet to near-infrared absorption spectrum of carbon dioxide ice from 0.174 to 1.8 μm. J. Geophys. Res. 110, E11003 https://doi.org/10.1029/2005JE002531.
Hansen, C.J., Byrne, S., Portyankina, G., Bourke, M., Dundas, C., McEwen, A., Mellon, M., Pommerol, A., Thomas, N., 2013. Observations of the northern seasonal polar cap on Mars: I. Spring sublimation activity and processes. Icarus 225, 881–897.
Hapke, B., 1981. Bidirectional reflectance spectroscopy: 1. Theory. J. Geophys. Res. Solid Earth 86 (B4), 3039–3054. https://doi.org/10.1029/JB086iB04p03039.
Harris, S., Rowan-Robinson, M., 1977. The brightest sources in the AFCRL survey. Astron. Astrophys. 60, 405–412.
Herr, K.C., Pimental, G.C., 1969. Infrared absorptions near three microns recorded over the polar cap of Mars. Science 166, 496–499.
Hess, S.L., Henry, R.M., Tillman, J.E., 1979. The seasonal variation of atmospheric pressure on Mars as affected by the south polar cap. J. Geophys. Res. 84, 2923–2927. https://doi.org/10.1029/JB084iB06p02923.
Hess, S.L., Ryan, J.A., Tillman, J.E., Henry, R.M., Leovy, C.B., 1980. The annual cycle of pressure on Mars measured by Viking landers 1 and 2. Geophys. Res. Lett. 7, 197–200. https://doi.org/10.1029/GL007i003p00197.
Iwasaki, K., Saito, Y., Akabane, T., 1986. Martian south polar cap 1973. Publ. Astron. Soc. Japan 38, 267–275.
James, P.B., Malolepszy, K.M., Martin, L.J., 1987. Interannual variability of Mars' south polar cap. Icarus 71, 298–305.
James, P.B., Martin, L.J., Henson, J.R., Birch, P.V., 1990. Seasonal recession of Mars' south polar cap in 1986. J. Geophys. Res. 95, 1337–1341.
Karatekin, Ö., Duron, J., Rosenblatt, P., Van Hoolst, T., Dehant, V., Barriot, J.P., 2005. Mars' time-variable gravity and its determination: simulated geodesy experiments. J. Geophys. Res. Planets 110, E06001. https://doi.org/10.1029/2004JE002378.
Karatekin, Ö., Dehant, V., Van Hoolst, T., 2006. Martian global-scale CO2 exchange from time-variable gravity measurements. J. Geophys. Res. (Planets) 111, E06003. https://doi.org/10.1029/2005JE002591.
Karatekin, Ö., de Viron, O., Lambert, S., Dehant, V., Rosenblatt, P., Van Hoolst, T., Le Maistre, S., 2011. Atmospheric angular momentum variations of Earth, Mars and Venus at seasonal time scales planet. Space Sci. 59, 923–933. https://doi.org/10.1016/j.pss.2010.09.010.
Kass, D.M., Schofield, J.T., Kleinböhl, A., McCleese, D.J., Heavens, N.G., Shirley, J.H., Steele, L.J., 2020. Mars climate sounder observation of Mars' 2018 global dust storm. Geophys. Res. Lett. 47, e2019GL083931 https://doi.org/10.1029/2019GL083931.
Kieffer, H.H., 1979. Mars south polar spring and summer temperatures: a residual CO2 frost. J. Geophys. Res. 84 (B14), 8263–8288.
Kieffer, H.H., Titus, T.N., Mullins, K.F., Christensen, P.R., 2000. Mars south polar spring and summer behavior observed by TES: seasonal cap evolution controlled by frost grain size. J. Geophys. Res. 105, 9653–9699. https://doi.org/10.1029/1999JE001136.
Kleinböhl, A., Spiga, A., Kass, D.M., Shirley, J.H., Millour, E., Montabone, L., Forget, F., 2020. Diurnal variations of dust during the 2018 global dust storm observed by the Mars Climate Sounder. J. Geophys. Res. Planets 125, e2019JE006115. https://doi.org/10.1029/2019JE006115.
Konopliv, A.S., Asmar, S.W., Folkner, W.M., Karatekin, Ö., Nunes, D.C., Smrekar, S.E., Yoder, C.F., Zuber, M.T., 2011. Mars high-resolution gravity fields from MRO, Mars seasonal gravity, and other dynamical parameters. Icarus 211 (1), 401–428.
Lange, L., Forget, F., Banfield, D., Wolff, M., Spiga, A., Millour, E., et al., 2022. Insight pressure data recalibration, and its application to the study of long-term pressure changes on Mars. J. Geophys. Res. Planets 127, e2022JE007190. https://doi.org/10.1029/2022JE007190.
Langevin, Y., Poulet, F., Bibring, J.-P., Schmitt, B., Doute, S., Gondet, B., 2005a. Summer evolution of the north polar cap of Mars as observed by OMEGA/Mars express. Science 307, 1581–1584.
Langevin, Y., Poulet, F., Bibring, J.-P., Gondet, B., 2005b. Sulfates in the north polar region of Mars detected by OMEGA/Mars express. Science 307, 1584–1586.
Langevin, Y., Bibring, J.-P., Montmessin, F., Forget, F., Vincendon, M., Douté, S., Gondet, B., 2007. Observations of the south seasonal cap of Mars during recession in 2004–2006 by the OMEGA visible/near-infrared imaging spectrometer on board Mars express. J. Geophys. Res. Planets 653 112 (E8).
Liuzzi, G., Villanueva, G.L., Mumma, M.J., Smith, M.D., Daerden, F., Ristic, B., Thomas, I., Vandaele, A.C., Patel, M.R., Lopez-Moreno, J.-J., et al., 2019. Methane on Mars: new insights into the sensitivity of CH4 with the NOMAD/ExoMars spectrometer through its first in-flight calibration. Icarus 321, 671–690.
Liuzzi, G., Villanueva, G.L., Crismani, M.M.J., Smith, M.D., Mumma, M.J., Daerden, F., et al., 2020. Strong variability of Martian water ice clouds during dust storms revealed from ExoMars trace gas orbiter/NOMAD. J. Geophys. Res. Planets 125. https://doi.org/10.1029/2019JE006250.
Liuzzi, G., Villanueva, G.L., Trompet, L., Crismani, M.M.J., Piccialli, A., Aoki, S., et al., 2021. First detection and thermal characterization of terminator CO2 ice clouds with ExoMars/NOMAD. Geophys. Res. Lett. 48, e2021GL095895.
López Valverde, M.-A., Funke, B., Brines, A., Stolzenbach, A., Modak, A., Hill, B., et al., 2022. Martian atmospheric temperature and density profiles during the 1st year of NOMAD/TGO solar occultation measurements. J. Geophys. Res. Planets 127, e2022JE007278. https://doi.org/10.1029/2022JE007278.
Määttänen, A., et al., 2010. Mapping the mesospheric CO2 clouds on Mars: MEx/OMEGA and MEx/HRSC observations and challenges for atmospheric models. Icarus 209, 452–469. https://doi.org/10.1016/j.icarus.2010.05.017.
Madeleine, J.-B., Forget, F., Millour, E., Montabone, L., Wolff, M.J., 2011. Revisiting the radiative impact of dust on Mars using the LMD global climate model. J. Geophys. Res. 116, E11010. https://doi.org/10.1029/2011JE003855.
Martínez, G.M., Newman, C.N., De Vicente-Retortillo, A., Fischer, E., Renno, N.O., Richardson, M.I., Fairén, A.G., Genzer, M., Guzewich, S.D., Haberle, R.M., Harri, A.-M., Kemppinen, O., Lemmon, M.T., Smith, M.D., de la Torre-Juárez, M., Vasavada, A. R., 2017. The modern near-surface Martian climate: a review of in-situ meteorological data from Viking to curiosity. Space Sci. Rev. 212, 295–338. https://doi.org/10.1007/s11214-017-0360-x.
Millour, E., Forget, F., Spiga, A., 2018. The Mars Climate Database, Version 5.3. ESAC, Madrid, Spain.
Montabone, L., Spiga, A., Kass, D.M., Kleinböhl, A., Forget, F., Millour, E., 2020. Martian year 34 column dust climatology from mars climate sounder observations: reconstructed maps and model simulations. J. Geophys. Res. - Planets. https://doi.org/10.1029/2019JE006111.
Montmessin, F., Bertaux, J.-L., Quémerais, E., Korablev, O., Rannou, P., Forget, F., Perrier, S., Fussen, D., Lebonnois, S., Rébérac, A., Dimarellis, E., 2006. Subvisible CO2 ice clouds detected in the mesosphere of Mars, 183 (2), 403–410.
Murchie, S., Kirkland, L., Erard, S., Mustard, J., Robinson, M., 2000. Near-infrared spectral variations of Martian surface materials from ISM imaging spectrometer data. Icarus 147, 44–471.
Montmessin, F., Gondet, B., Bibring, J., Langevin, Y., Drossart, P., Forget, F., Fouchet, T., 2007. Hyperspectral imaging of convec-tive CO2 ice clouds in the equatorial mesosphere of Mars. J. Geophys. Res. Planets 112, E11S90.
Murchie, S., Arvidson, R., Bedini, P., Beisser, K., Bibring, J.P., Bishop, J., et al., 2007. Compact reconnaissance imaging spectrometer for Mars (CRISM) on Mars reconnaissance orbiter (MRO). J. Geophys. Res. 112 (E5), E05S03. https://doi.org/10.1029/2006JE002682.
Neefs, E., Vandaele, A.C., Drummond, R., Thomas, I.R., Berkenbosch, S., Clairquin, R., Delanoye, S., Ristic, B., Maes, J., Bonnewijn, S., et al., 2015. NOMAD spectrometer on the ExoMars trace gas orbiter mission: Part1—design, manufacturing and testing of the infrared channels. Appl. Opt. 54, 8494–8520.
Oliva, F., D'Aversa, E., Bellucci, G., Carrozzo, F.G., Ruiz Lozano, L., Altieri, F., et al., 2022. Martian CO2 ice observation at high spectral resolution with ExoMars/TGO NOMAD. J. Geophys. Res. Planets 127, e2021JE007083.
Patel, M.R., Antoine, P., Mason, J.P., Leese, M.R., Hathi, B., Stevens, A.H., Dawson, D., Gow, J.P.D., Ringrose, T.J., Holmes, J.A., et al., 2017. NOMAD spectrometer on the ExoMars trace gas orbiter mission: part 2—design, manufacturing, and testing of the ultraviolet and visible channel. Appl. Opt. 56, 2771–2782.
Pelkey, S.M., et al., 2007. CRISM multispectral summary products: parameterizing mineral diversity on Mars from reflectance. J. Geophys. Res. 112, E08S14 https://doi.org/10.1029/2006JE002831.
Piqueux, S., Byrne, S., Richardson, M.I., 2003. Sublimation of Mars's southern seasonal CO2 ice cap and the formation of spiders. J. Geophys. Res. 108, 5084.
Piqueux, S., Kleinböhl, A., Hayne, P.O., Kass, D.M., Schofield, J.T., McCleese, D.J., 2015. Variability of the Martian seasonal CO2 cap extent over eight Mars years. Icarus 251, 164–180. ISSN 0019-1035,. https://doi.org/10.1016/j.icarus.2014.10.045. ISSN 0019-1035,.
Riu, L., Poulet, F., Carter, J., Bibring, J.-P., Gondet, B., Vincendon, M., 2019. The M3 project: 1—a global hyperspectral image-cube of the Martian surface. Icarus 319, 281–292.
Rodgers, C.D., 2000. Inverse methods for atmospheric sounding. Series Atmos. Ocean. Planet. Phys. 2 https://www.worldscientific.com/worldscibooks/, doi:10.1142/3171.
Ruiz Lozano, L., Karatekin, Ö., Dehant, V., Bellucci, G., Oliva, F., D'Aversa, E., Carrozzo, F.G., Altieri, F., Thomas, I.R., Willame, Y., Robert, S., Vandaele, A.C., Daerden, F., Ristic, B., Patel, M.R., López Moreno, J.J., 2022. Evaluation of the capability of ExoMars-TGO NOMAD infrared nadir channel for water ice clouds detection on Mars. Remote Sens. 14, 4143.
Schmidt, F., Douté, S., Schmitt, B., Vincendon, M., Bibring, J.-P., Langevin, Y., OMEGA Team, 2009. Albedo control of seasonal south polar cap recession on Mars. Icarus 200, 374–394.
Schmidt, F., Schmitt, B., Douté, S., Forget, F., Jian, J.J., Martin, P., Langevin, Y., Bibring, J.P., OMEGA Team, 2010. Sublimation of the martian CO2 seasonal south polar cap. Planet. Space Sci. 58, 1129–1138.
Singh, D., Flanner, M.G., 2016. An improved carbon dioxide snow spectral albedo model: application to Martian conditions. J. Geophys. Res. Planets 121 (10), 2037–2054.
Smith, D.E., et al., 1999. The global topography of Mars and implications for surface evolution. Science 284 (5419), 1495–1503. https://doi.org/10.1126/science.284.5419.1495.
Stamnes, K., Thomas, G.E., Stamnes, J.J., 2017. Radiative Transfer in the Atmosphere and Ocean. Cambridge University Press, Cambridge. https://doi.org/10.1017/9781316148549.

Streeter, P.M., Lewis, S.R., Patel, M.R., Holmes, J.A., Kass, D.M., 2020. Surface warming during the 2018/Mars year 34 global dust storm. Geophys. Res. Lett. 47, e2019GL083936 https://doi.org/10.1029/2019GL083936.

Thomas, I.R., Vandaele, A., Robert, S., Neefs, E., Drummond, R., Daerden, F., Delanoye, S., Ristic, B., Berkenbosch, S., Clairquin, R., 2016. Optical and radiometric models of the NOMAD instrument part II: the infrared channels-SO and LNO. Opt. Express 24, 3790–3805.

Thomas, I.R., Shohei, A., Trompet, L., Robert, S., Depiesse, C., Willame, Y., Cruz-Mermy, G., Schmidt, F., Erwin, J.T., Vandaele, A.C., et al., 2022. Calibration of NOMAD on ESA's ExoMars trace gas orbiter: part 2—the limb, nadir and occultation (LNO) channel. Planet. Space Sci. 218, 105410.

Titus, T., Kieffer, H., 2002. A Comparison of the Mars South Polar Recession Rates Between 1999 and 2001.

Van den Acker, E., Van Hoolst, T., de Viron, O., Defraigne, P., Dehant, V., Forget, F., Hourdin, F., 2002. Influence of the winds and of the CO2 mass exchange between the atmosphere and the polar ice caps on Mars' orientation parameters. J. Geophys. Res. (Planets) 107 (E7). https://doi.org/10.1029/2000JE001539, 9–1, CiteID 5055.

Vandaele, A., Neefs, E., Drummond, R., Thomas, I., Daerden, F., Lopez-Moreno, J.-J., Rodriguez, J., Patel, M., Bellucci, G., Allen, M., et al., 2015a. Science objectives and performances of NOMAD, a spectrometer suite for the ExoMars TGO mission. Planet. Space Sci. 119, 233–249.

Vandaele, A.C., Willame, Y., Depiesse, C., Thomas, I.R., Robert, S., Bolsée, D., Patel, M. R., Mason, J.P., Leese, M., Lesschaeve, S., et al., 2015b. Optical and radiometric models of the nomad instrument part I: the UVIS channel. Opt. Express 23, 30028–30042.

Vandaele, A.C., Lopez-Moreno, J.-J., Patel, M.R., Bellucci, G., Daerden, F., Ristic, B., Robert, S., Thomas, I.R., Wilquet, V., Allen, M., Alonso-Rodrigo, G., Altieri, F., Aoki, S., Bolsée, D., Clancy, T., Cloutis, E., Depiesse, C., Drummond, R., Fedorova, A., Formisano, V., Funke, B., González-Galindo, F., Geminale, A., Gérard, J.-C., Giuranna, M., Hetey, L., Ignatiev, N., Kaminski, J., Karatekin, O., Kasaba, Y., Leese, M., Lefèvre, F., Lewis, S.R., López-Puertas, M., López-Valverde, M., Mahieux, A., Mason, J., McConnell, J., Mumma, M., Neary, L., Neefs, E., Renotte, E., Rodriguez-Gomez, J., Sindoni, G., Smith, M., Stiepen, A., Trokhimovsky, A., Vander Auwera, J., Villanueva, G., Viscardy, S., Whiteway, J., Willame, Y., Wolff, M., the NOMAD Team, 2018. NOMAD, an integrated suite of three spectrometers for the ExoMars trace gas Mission: technical description, science objectives and expected performance. Space Sci. Rev. 214 (5), 80.

Villanueva, G.L., Smith, M.D., Protopapa, S., Faggi, S., Mandell, A.M., 2018. Planetary Spectrum generator: an accurate online radiative transfer suite for atmospheres, comets, small bodies and exoplanets. J. Quant. Spectrosc. Radiat. Transf. 217, 86–104.

Vincendon, M., Pilorget, C., Gondet, B., Murchie, S., Bibring, J.-P., 2011. New near-IR observations of mesospheric CO2 and H2O clouds on Mars. J. Geophys. Res. 116, E00J02. https://doi.org/10.1029/2011JE003827.

Viúdez-Moreiras, D., Newman, C.E., de la Torre, M., Martínez, G., Guzewich, S., Lemmon, M., et al., 2019. Effects of the MY34/2018 global dust storm as measured by MSL REMS in Gale crater. J. Geophys. Res. Planets 124, 1899–1912. https://doi.org/10.1029/2019JE005985.

Viviano, C.E., Seelos, F.P., Murchie, S.L., Kahn, E.G., Seelos, K.D., Taylor, H.W., Taylor, K., Ehlmann, B.L., Wiseman, S.M., Mustard, J.F., et al., 2014. Revised CRISM spectral parameters and summary products based on the currently detected mineral diversity on Mars. J. Geophys. Res. Planets 119, 1403–1431.

Warren, S.G., Brandt, R.E., 2008. Optical constants of ice from the ultraviolet to the microwave: a revised compilation. J. Geophys. Res. 113, D14220. https://doi.org/10.1029/2007JD009744.

Wolff, M.J., Smith, M.D., Clancy, R.T., Arvidson, R., Kahre, M., Seelos, F., et al., 2009. Wavelength dependence of dust aerosol single scattering albedo as observed by the compact reconnaissance imaging spectrometer. J. Geophys. Res. 114, E00D04. https://doi.org/10.1029/2009JE003350.

Wolff, M.J., Clancy, R.T., Kahre, M.A., Haberle, R.M., Forget, F., Cantor, B.A., Malin, M. C., 2019. Mapping water ice clouds on Mars with MRO/MARCI. Icarus 332, 24–49.

Wolkenberg, P., Giuranna, M., Grassi, D., Aronica, A., Aoki, S., Scaccabarozzi, D., Saggin, B., 2018. Characterization of dust activity on Mars from MY27 to MY32 by PFS-MEX observations. Icarus 310, 32–47. https://doi.org/10.1016/j.icarus.2017.10.045.

Wolkenberg, P., Giuranna, M., Smith, M.D., Grassi, D., Amoroso, M., 2020. Similarities and differences of global dust storms in MY 25, 28, and 34. J. Geophys. Res. Planets 125, e2019JE006104. https://doi.org/10.1029/2019JE006104.